A constitutive framework for caprocks accounting for viscoplastic cyclic degradation and coupled geo-chemo-mechanical processes

Geomechanics for Energy and the Environment 42 (2025) 100689

Contents lists available at ScienceDirect

Geomechanics for Energy and the Environment

journal homepage: www.elsevier.com/locate/gete

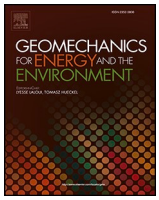

A constitutive framework for caprocks accounting for viscoplastic cyclic degradation and coupled geo-chemo-mechanical processes

Andrea Ciancimino [a,*], Trishala Daka [a], Liliana Gramegna [b], Guido Musso [a], Giorgio Volonté [c], Gabriele Della Vecchia [b]

[a] Politecnico di Torino, Department of Structural, Building and Geotechnical Engineering, Corso Duca degli Abruzzi 24, Turin 10129, Italy
[b] Politecnico di Milano, Department of Civil and Environmental Engineering, Piazza Leonardo da Vinci, 32, Milano 20133, Italy
[c] ENI S.p.A., Reservoir and Petroleum Engineering Laboratories (Geomechanics), via Maritano 26, Milano, San Donato M.se 20097, Italy

ARTICLE INFO

Keywords:
Energy geomechanics
Degradation
Caprock
CO_2 storage
Gas storage
Cyclic loading

ABSTRACT

This paper provides an extension of an existing elasto-plastic framework originally proposed by Gens & Nova (1993) for modelling the response of structured soils and soft rocks. The model is enhanced to reproduce not only the mechanical response of caprocks under standard monotonic triaxial loading, but also the effects of the environmental and hydraulic loading induced by modern energy applications, including gas/hydrogen storage and geological carbon storage. The novelty of these applications, compared to the more usual ones developed by the oil and gas industry over decades, lies in the complex pore fluid and stress pressure histories applied and in the strong geochemical interaction of the rock formations with non-native fluids. Cyclic pore pressure histories due to seasonal gas storage may result in a mechanical degradation of the caprock material, while chemical degradation may occur due to pore water acidification resulting from the rock-water-CO_2 interaction. To cope with the cyclic mechanical degradation, the framework is first coupled with the extended overstress theory, so to satisfactorily reproduce the time-dependent behaviour of caprocks, which presents inelastic strains even within the yield surface. Such an extension is shown to be essential to reproduce the strong strain-rate dependence and the increase in the number of cycles to failure with the amplitude of cyclic loading observed in experimental data obtained on intact specimens of an Italian stiff carbonatic clay. The elasto-plastic model is then enhanced to account for chemical degradation, using the calcite mass fraction dissolution as a variable controlling damage evolution. Combined with a geochemical reactive transport model, this extension satisfactorily reproduces the progressive degradation of a Chinese shale due to CO_2 exposure, showing the ability of the framework to model coupled geo-chemo-mechanical processes.

1. Introduction

Actions against global warming and the responsible use of energy resources are two fundamental needs that society is facing today, and the energy sector in particular. Many of the emerging applications of energy geomechanics are related to the storage of non-native fluids in geological formations at high depths.[1] Depleted hydrocarbon reservoirs and saline aquifers are currently being considered or used for the permanent storage of supercritical CO_2 and Underground Gas Storage (UGS, the seasonal storage of natural gas), and also for the temporary storage of green and blue hydrogen.[2–5] When a fluid, largely immiscible with water, is injected into a porous geological formation, different geomechanical issues can emerge. Such issues are a consequence of the complex and extreme conditions imposed by the engineering operations, involving coupled mechanical, geochemical, hydraulic, and thermal processes.

Fluid injection into a depleted reservoir or a saline aquifer causes an increase in the pore pressure, which promotes the expansion of the host formation. Displacements propagate towards the surface, resulting in progressive changes to the mean effective stress and the deviatoric stress of the caprock.[6–8] The picture is more complex in UGS or hydrogen storage operations, where gas is cyclically produced from the reservoir, typically reducing the deviatoric stress in the caprock.[9–12] A combination of storage/production histories will therefore result in cyclic stress paths, which might induce fatigue phenomena. On the other hand, when depleted hydrocarbon reservoirs are used for carbon capture and storage

* Corresponding author.
E-mail address: andrea.ciancimino@polito.it (A. Ciancimino).

https://doi.org/10.1016/j.gete.2025.100689
Received 30 April 2024; Received in revised form 21 May 2025; Accepted 24 May 2025
Available online 26 May 2025

operations, CO_2 can dissolve in the native brine, creating an acid plume that can last for thousands of years,[13,14] diffuse into the caprock and trigger geochemical reactions,[15] depending on both the chemistry of the brine and the rock mineralogy. In turn, geochemical reactions can induce changes in porosity, permeability, and mechanical behaviour of the caprock formation.[16–20]

Storage in underground reservoirs can only be effective if the geological strata overlying the reservoir/aquifer provide adequate sealing. Indeed, mechanical failure of the caprock could result in the opening of fractures, generating preferential flow paths through which the fluids could leak to the surface.[21] To ensure adequate sealing capacity, the caprock must therefore be continuous and integer, and its threshold capillary pressure (i.e. the capillary pressure above which the non-wetting fluid starts flowing through its pores) must exceed the difference between the pressure of the injected fluid and that of the water saturating its pores.[6,22–24] Robust modelling of the caprock mechanical behaviour is thus a fundamental requirement for safe storage due to the complex hydro-chemo-mechanical histories imposed by engineering operations.

Caprocks are either evaporites or sedimentary clayey rocks. Both damage mechanics and elasto-plasticity have been used to reproduce the stress-strain response of these materials.[25–28] In the context of elasto-plasticity, the constitutive reference for bonded soils and weak rocks is provided by the pioneering frame of Gens and Nova.[29] Different models have been later published based on such, or similar, concepts.[30–35] However, unlike the available literature for structured materials which deals with shallow applications,[36–39] fluid storage at high depths requires accounting for the effects of high stresses with the concomitant action of cyclic loadings and the transport of chemicals which, by reacting with the certain minerals forming the caprock, may lead to progressive chemical degradation.

When cyclic loadings are of concern, constitutive models need to be able to reproduce several complex aspects of the cyclic response of structured geomaterials, such as small-strain stiffness, nonlinearity, irreversibility of strains under cyclic loading, elastic and inelastic anisotropy, coupling between shear and volumetric strains, time dependency, initial structure degree and cyclic destructuration.[40–43] Among the various possible modelling strategies, an effective approach is represented by bounding surface plasticity models.[44–47] In this framework, the elastic behaviour is limited to a nucleus, typically characterised by a very small size. Beyond this nucleus, the response is always elasto-plastic, with a plastic modulus depending on the distance between the current stress state and the image stress state located on the bounding surface. As a consequence, the application of a given cyclic stress path is likely to lead to an accumulation of plastic strains, which can therefore be coupled with a destructuration mechanism to capture cyclic degradation.[40,48] At present, the use of constitutive models for structured materials has been devoted mainly to applications dealing with relatively shallow materials under low stresses, such as seismic applications, offshore foundations, and cyclic response of soil embankments.[48–50] These applications involve cyclic histories characterized by relatively short loading periods, for which it is reasonable to assume negligible viscous strains. Conversely, the characteristic periods of UGS operations match the seasonal and annual timescales of energy applications.[3,51] Therefore, the time-dependent mechanical response typical of structured geomaterials[52–55] starts to play a role.

Applications involving geochemical processes, such as carbon capture and storage operations, require an extension of the modelling framework to capture material degradation induced by chemical reactions. A possible modelling strategy, as suggested for example by Lagioia and Nova[56] and Nova et al.,[30] is to rely on a purely phenomenological approach, i.e. to link the evolution of internal variables to the damage induced by acidification. The latter can be quantified by a chemical variable introduced into the mechanical model, which must be estimated by reference to appropriate geochemical models.[57] An interesting alternative is represented by models inspired by micromechanical considerations,[34,35,58] which consider a specific microstructure characterised by either reactive grains and reactive bonds or non-reactive grains and reactive bonds. Although it is useful to gain insight into the role of chemical dissolution on the mechanical behaviour of certain types of soft rocks (e.g. calcarenites), the mineralogical complexity of natural caprocks strongly suggests the implementation of a purely phenomenological approach due to the inherent difficulties in identifying a specific damage mechanism, which can be more complex than bond dissolution.[59]

In this paper, the suitability of elasto-plasticity with destructuration for fluid storage at high depths is assessed by adopting the phenomenological framework introduced by Gens and Nova.[29] The framework is extended to take into account the time dependence of the mechanical response and/or its coupling with geo-chemical processes, to meet the emerging applications in the field of energy geomechanics described above. Either the fabric or the bonds between the clay matrix associated with granular inclusions are considered to increase the size of the yield surface of the unstructured material. The latter is modelled according to classic elastoplastic models for soils, whose parameters can be determined directly by laboratory testing. Nevertheless, alternative strategies that account for the influence of the different solid phases could be employed. In such approaches, the macroscopic behaviour of soft rocks is derived from the upscaling of the properties of the clay matrix and the grain inclusions. For instance, Borja et al.[60] modelled the response of shales within the framework of Cam Clay hardening plasticity, also considering heterogeneity and anisotropy. Farhat et al.[61] applied a nonlinear homogenization method to determine the properties of the representative element volume, upscaling the mesoscopic viscous and elastoplastic properties.

The capability of the framework to reproduce the mechanical behaviour of two structured stiff clays under high confinements is firstly checked. These preliminary analyses are of interest to mimic monotonic loading of the caprock, e.g. due to high-pressure increments in the reservoirs, such as those that could be imparted when the fluid is stored for the first time. The reliability of the framework is then checked for the case of cyclic loadings, such as those caused by seasonal storage/production of natural gas or hydrogen. Model predictions are compared to the experimental results of cyclic tests aimed at assessing the fatigue life of an Italian stiff carbonatic clay. The experimental results showed a relevant effect of the applied strain-rate, which was accounted for by introducing a viscous strain component. The latter can be modelled through different approaches. For instance, Borja et al.[60] and Sari et al.[62] rely on the basic assumption of the classical overstress theory.[63,64] The viscosity parameter adopted by Borja et al.[60] is phenomenological, whereas Sari et al.[62] relate viscosity to activation enthalpy. However, in the overstress theory, viscoplastic strains are only activated if the current stress state lies on or outside the yield surface (i.e. when the value of the yield function is $f \geq 0$). On the contrary, experimental evidence on shales and carbonatic rocks shows that creep strains develop even at relatively low stresses,[65,66] well within the yield surface,[67] and that peak strength and stress-strain relationship before failure are also strain-rate dependent.[54,55] In this study, the Gens and Nova[29] framework is enhanced according to the extended overstress theory, which also models viscous strains when $f < 0$, i.e. when the stress state is within a reference yield surface associated with a fixed strain-rate.[68–70] The viscosity parameter is defined based on laboratory tests on the unstructured material, in analogy with the Gens and Nova[29] approach, although micro-mechanical techniques such as the one proposed by Farhat et al.[61] could also be adopted without affecting the model conceptualization.

Finally, chemical degradation is implemented to predict the long-term effects that can descend from the reactive transport of dissolved CO_2 in the caprock. The framework, coupled with geochemical reactive transport analyses, provides a versatile tool to account for the chemical degradation of the caprock. The proposed model is based on the introduction of a single scalar damage variable at the phenomenological level so that the coupling with the FEM reactive transport model allows the

consideration of any realistic chemo-hydraulic scenario involving rock-brine-CO_2 interactions. After a brief review of the geochemical processes induced by CO_2 injection and dissolution, a procedure is proposed to feed the elasto-plastic model with information from geochemical finite element numerical simulations to reproduce the induced changes in material elastic stiffness and internal variables. Model predictions are then compared to experimental data for a shale from the literature, which was exposed to CO_2 before mechanical testing.

2. Elasto-plasticity as a constitutive framework for the mechanical behaviour of caprock materials

Hardening elasto-plasticity has proved to be a successful framework to model the mechanical behaviour of soft rocks and structured soils, as introduced by Gens and Nova.[29] The framework is based on the experimental observation that natural soils and soft sedimentary rocks have a peculiar mechanical behaviour with respect to remoulded soils, due to the fabric and the bonds between the grains, which convey a stiffer mechanical response at low strain levels, a larger shear strength and non-negligible tensile strength. When bonds are destroyed upon mechanical loading, the metastability of the material structure becomes evident and the compressibility becomes larger than the remoulded soil one. A brief description of the framework is provided, together with a comparison of model predictions with experimental data regarding one shale and one stiff carbonatic clay which serves as caprock.

2.1. Elasto-plastic constitutive framework for remoulded caprock materials

According to the theory of small-strain elasto-plasticity, the strain tensor increment $d\boldsymbol{\varepsilon}$ can be written as the sum of an elastic $d\boldsymbol{\varepsilon}^{\mathbf{e}}$ and a plastic $d\boldsymbol{\varepsilon}^{\mathbf{p}}$ component:

$$d\varepsilon_{ij} = d\varepsilon^{e}_{ij} + d\varepsilon^{p}_{ij} \tag{1}$$

It is worth mentioning that hereafter, the notation 'd' indicates an infinitesimal increment of the variable, where time plays no explicit role. Because elastic strains are assumed to develop whenever there is a change in effective stress, the elastic constitutive relation reads:

$$d\sigma'_{kh} = D^{e}_{khij} d\varepsilon^{e}_{ij} = D^{e}_{khij}\left(d\varepsilon_{ij} - d\varepsilon^{p}_{ij}\right) \tag{2}$$

where $d\sigma'_{kh}$ is the effective stress increment and D^{e}_{khij} is the elastic stiffness tensor. The experimental evidence of the stiff and reversible responses upon initial loading of caprock materials can be reproduced via the introduction of a yield surface $f(\sigma'_{ij}, \psi_k) = 0$, which has the role of delimiting the elastic domain. In hardening elasto-plasticity, the yield surface is expressed as a scalar function of the stress tensor σ'_{ij} and of a set of internal variables, ψ_k. The plastic strain increment is written as:

$$d\varepsilon^{p}_{rs} = \Lambda \frac{\partial g}{\partial \sigma'_{rs}} \tag{3}$$

where Λ is a non-negative scalar (plastic multiplier) and g is a function of the current stress state. According to the classical requirement of strain-hardening plasticity, the definition of the hardening function is also required, linking the evolution of the internal variables with the plastic strain increment:

$$d\psi_k(\varepsilon^{p}_{rs}) = \frac{\partial \psi_k}{\partial \varepsilon^{p}_{rs}} d\varepsilon^{p}_{rs} \tag{4}$$

In the following, a simple elasto-plastic model for the unstructured material is adopted, relying on classical assumptions, including: (*i*) non-linear elastic law, with a mean effective stress dependence for the bulk modulus; (*ii*) yield function dependent on just one scalar internal variable, p_c, i.e. the preconsolidation pressure of the material; (*iii*) non-associative flow rule, i.e. $f \neq g$; (*iv*) volumetric and deviatoric hardening, i.e. p_c evolves as a function of both volumetric and deviatoric plastic strain increments. The following equations are here adopted, among several proposals available in the literature.[34,35,71] For the sake of simplicity, the axis-symmetric formulation in terms of the mean effective stress p', and the deviatioric stress q, is here presented, with their conjugate strain variables volumetric strain ε_{vol} and deviatoric strain ε_{dev} (see, e.g., [72]).

As for the elastic behaviour, isotropic non-linear elasticity is adopted:

$$\begin{bmatrix} d\varepsilon^{e}_{vol} \\ d\varepsilon^{e}_{dev} \end{bmatrix} = \begin{bmatrix} 1/K & 0 \\ 0 & 1/3G \end{bmatrix} \begin{bmatrix} dp' \\ dq \end{bmatrix} \tag{5}$$

where the bulk modulus K is assumed to depend on the mean effective stress, on void ratio and on the logarithmic elastic compressibility κ according to $K = \frac{(1+e)p'}{\kappa}$, and the shear modulus G is kept constant. The yield surface is expressed according to Panteghini and Lagioia:[73]

$$f = \frac{q^2}{M^2} \frac{\left[p'(1-2\alpha_y) + \alpha_y p_c\right]^2}{4p_c^2(1-\alpha_y)\alpha_y{}^3} - p'(p_c - p') \tag{6}$$

where α_y and M are material parameters influencing the shape of the yield surface. In particular, M is the critical state stress ratio. As in the Modified Cam Clay model, an isotropic hardening law is used to describe the evolution of the yield surface:

$$dp_c = \frac{1+e_0}{\lambda - \kappa} p_c d\varepsilon^{p}_{vol} \tag{7}$$

in which e_0 is the initial void ratio, and κ and λ are respectively the elastic and elasto-plastic compressibility coefficients. The plastic potential is expressed with a function similar to the yield function, allowing the possibility of using both an associated and a non-associated flow rule depending on the parameter β_y:

$$g = \beta_y \frac{q^2}{M^2} \frac{\left[p'(1-2\alpha_y) + \alpha_y p_c\right]^2}{4p_c^2(1-\alpha_y)\alpha_y{}^3} - p'(p_c - p') \tag{8}$$

The model was implemented in a constitutive driver, following the numerical integration scheme depicted in Cattaneo et al.[74]

2.2. Elasto-plastic constitutive framework for natural caprock materials

Material structure is known to modify both the stiffness and the strength of caprock materials. A body of experimental data ([56,75] among others) has shown the impact of structure on compression paths, including the increase of yield stress and the inelastic compressibility upon debonding. When shear paths are of concern, the presence of bonding also provides cohesion, peak strength, and relevant softening upon debonding. The key element in reproducing the constitutive behaviour of natural sedimentary caprocks is thus the concept of structure/destructuration and its mathematical representation. In the phenomenological framework proposed by Gens and Nova,[29] the material structure (intended here as a combination of fabric and interparticle bonding) is introduced through a scalar measure b evolving upon mechanical loading. The preconsolidation pressure in the presence of structure p_{cb} and the tensile strength p_t can be linked to b, via two functions, $f_c(b)$ and $f_t(b)$, as:

$$\frac{p_{cb}}{p_c} = f_c(b) \tag{9}$$

$$\frac{p_t}{p_c} = f_t(b) \tag{10}$$

where p_c is the preconsolidation pressure for the remoulded material ($b = 0$). Of course, p_{cb} must tend to p_c and p_t must tend to zero in the destructured condition. In general, b is assumed to evolve as a function

of another scalar variable, i.e. the damage h.[29]. The link between these two variables is provided by a suitable decreasing function $b = b(h)$. If just mechanical loading is considered and keeping the framework of elasto-plasticity, the function h should in turn depend on the plastic strain increment. Under these assumptions, the addition of structure/destructuration to a strain-hardening elasto-plastic constitutive model is straightforward, as described in the following.

To account for the effect of the structure on both preconsolidation pressure and tensile strength, Eq. 6 can be modified as:

$$f = \frac{q^2}{M^2}\frac{\left[(p'+p_t)(1-2\alpha_y)+\alpha_y(p_{cb}+p_t)\right]^2}{4(p_{cb}+p_t)^2(1-\alpha_y)\alpha_y^3} - (p'+p_t)(p_{cb}-p') \tag{11}$$

Similarly, the plastic potential (Eq. 8) can be rewritten as:

$$g = \beta_y\frac{q^2}{M^2}\frac{\left[(p'+p_t)(1-2\alpha_y)+(p_{cb}+p_t)\right]^2}{4(p_{cb}+p_t)^2(1-\alpha_y)\alpha_y^3} - (p'+p_t)(p_{cb}-p') \tag{12}$$

The role of structure on p_{cb} and p_t is here simply expressed as in Gens and Nova:[29]

$$f_c(b) = \frac{p_{cb}}{p_c} = 1 + b \tag{13}$$

$$f_t(b) = \frac{p_t}{p_c} = \alpha_t b \tag{14}$$

as well as the monotonic decrease of b related to damage increase could be simply calculated by the following equation:

$$b = b_0 e^{-(h-h_0)} \tag{15}$$

where b_0 and h_0 are the initial values of the structure degree and the damage variables. The proposal of Gajo et al.[35] is finally used to link the increment of the damage variable with the plastic strain increment, as:

$$\mathrm{d}h = h_{dev}\left|\mathrm{d}\varepsilon^p_{dev}\right| + h_{vol}\left|\mathrm{d}\varepsilon^p_{vol}\right| \tag{16}$$

being h_{dev} and h_{vol} two material parameters. Eq. 7 provides the relationship between $\mathrm{d}p_c$ and plastic strains.

According to the framework discussed, the yield surface evolution is controlled by both plastic hardening of the remoulded material (Eq. 7) and structure degradation (Eq. 15). Being the two mechanisms related to plastic strain increments, the classical methods of computational plasticity can be adopted, leading to the definition of a hardening modulus[30] that formally consists of two competing factors:

$$H = H_s + H_d \tag{17}$$

where H_s corresponds to the enlargement/reduction of the elastic domain for the remoulded soil, while H_d accounts for the reduction of yield surface related to degradation.

Finally, natural sedimentary caprocks are often characterized by bedding planes with different properties, which convey an elastic cross-anisotropic behaviour to the material at the representative elementary volume level. Under undrained conditions, this anisotropic behaviour results in inclined effective stress paths upon shearing. This can be simply accounted for according to the proposal of Graham and Houlsby;[76] accordingly, the elastic compliance matrix can be written as:

$$\begin{bmatrix}\mathrm{d}\varepsilon^e_{vol}\\ \mathrm{d}\varepsilon^e_{d}\end{bmatrix} = \begin{bmatrix}-G^*/(J^2-K^*G^*) & J/(J^2-K^*G^*)\\ J/(J^2-K^*G^*) & -K^*/(J^2-K^*G^*)\end{bmatrix}\begin{bmatrix}\mathrm{d}p'\\ \mathrm{d}q\end{bmatrix} \tag{18}$$

where K^* and G^* are the bulk modulus and the shear modulus modified by anisotropy and J express the cross-link between a change of deviator strain and a change of mean stress p'. Parameters in Eq. 18 can be linked to the vertical Young modulus $E_v = E^*$, to the Poisson ratio due to vertical loading $\nu_{vh} = \nu^*$ and to the anisotropy parameter $E_h/E_v = \alpha^2$ as:

$$K^* = E^*\frac{1}{3(1-2\nu^*)} \tag{19}$$

$$G^* = E^*\frac{2-2\nu^*-4\alpha\nu^*+\alpha^2}{6(1+\nu^*)(1-2\nu^*)} \tag{20}$$

$$J = E^*\frac{1-\nu^*+\alpha\nu^*-\alpha^2}{3(1+\nu^*)(1-2\nu^*)} \tag{21}$$

2.3. Simulation of monotonic triaxial tests of caprock materials

The capabilities of the framework were checked with experimental data of triaxial tests performed on two intact structured clayey soft rocks, namely the Opalinus and the Santerno Clay. The values of the model parameters adopted in the simulations for both the materials are provided in Table 1.

Experimental data on intact Opalinus Clay, an over-consolidated shale formation formed as a marine sediment and consisting of fine mud particles, were presented in Giger et al.[77] After the consolidation stage (consolidation pressures ranging from 16.5 MPa to 51.5 MPa), the deviatoric loading was applied in undrained conditions using a constant loading rate of $1.2\bullet10^{-4}$%/min. Experimental results and model predictions are shown in Fig. 1. The initial leftward inclination of the stress path in the $q-p'$ plane suggests a cross-anisotropic response, as reflected by the calibrated value of $\alpha = 1.1$. Such a value is in agreement with several experimental studies that report an inherent anisotropy for the Opanlinus clay, resulting from its stratification process, which leads to a higher elastic modulus in the horizontal direction (i.e. parallel to the bedding planes) than in the vertical direction.[78–80] The brittle behaviour with post-peak softening is well reproduced by the model. The predictions in terms of maximum deviator stress and ultimate strength are satisfactory, as well as the peculiar response in the $q-p'$ plane, related to the predicted dilatant response and pore pressure build-up. Due to the mathematical nature of the elasto-plastic model, the elastic law adopted is not able to reproduce the dependency of the elastic shear modulus on the confining pressure, as well as the pre-peak bending over the stage before the peak in deviator stress.

The model was then adopted to simulate the experimental data obtained from intact specimens of a plio-pleistocenic Italian caprock known as "Argille del Santerno" (termed as Santerno Clay, data after [81]). It can be classified as clay (49.6 %) with silt (49.5 %) with a plasticity index $PI = 18$ % (being the liquid limit $w_L = 43$ % and the plastic limit $w_P = 25$ %). The material is known to be particularly stiff, also due to the high content of carbonate minerals (calcite fraction of 28 % and dolomite fraction of 11 %). Intact samples were cored from a deep layer above a hydrocarbon reservoir, at a depth of about 1150 m. A detailed description of the specimen preparation procedures, together with an in-depth analysis of the representativeness of the intact material can be found in Ciancimino et al.[81]

Two triaxial tests were considered, having an anisotropic consolidation stage with ratio $q/p' = 0.78$, followed by undrained shearing with an axial strain-rate of 0.01 %/min: (*i*) sample IN1, consolidated to $p' = 8.1$ MPa and $q = 6.3$ MPa; (*ii*) sample IN2, consolidated to $p' = 16.2$ MPa and $q = 12.6$ MPa. Due to the geological history of Santerno Clay, it is possible to state that the consolidation stage was completely performed inside the elastic domain. Data from the following undrained shear stage are shown in Fig. 2. The initial stage of the stress path in the $q-p'$ plane (Fig. 2b) again reveals evidence of anisotropy, suggesting in this case larger stiffness in the vertical direction. Such a response can be explained by the fact that rocks[82,83] and claystones[84] often exhibit significant dilatant behaviour upon deviatoric loading, even before reaching peak shear strength. In the triaxial tests considered here, Santerno clay specimens were anisotropically consolidated with an initial stress obliquity of $q/p' = 0.78$. Consequently, the dilatant material response prevailed from the beginning of the tests, resulting in a

Table 1
Model parameters and initial values of the internal variables used in the simulations of the undrained triaxial tests on intact Opalinus Clay and Santerno Clay.

	κ	G	α	λ	M	α_y	β_y	p_{c0}	b_0	h_0	α_t	h_{dev}	h_{vol}
	(-)	(MPa)	(-)	(-)	(-)	(-)	(-)	(MPa)	(-)	(-)	(-)	(-)	(-)
Opalinus Clay	0.04	900	1.1	0.053	0.78	0.7	0.7	15	6.2	0	0	7	90
Santerno Clay	0.033	300	0.83	0.102	1	0.62	1.1	13.5	1.2	0	0	2.5	90

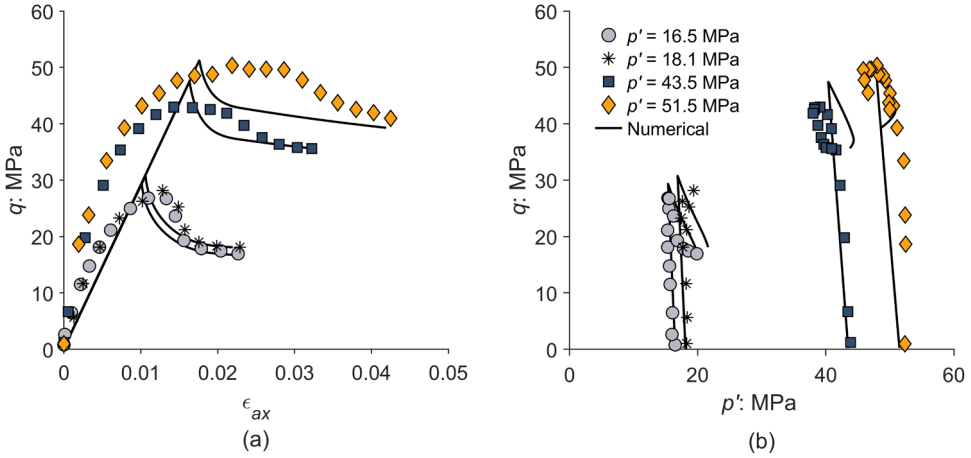

Fig. 1. Comparison between model predictions and experimental data for the intact Opalinus Clay in undrained triaxial tests: (a) deviatoric stress-strain curves; and (b) effective stress paths (data after [77]).

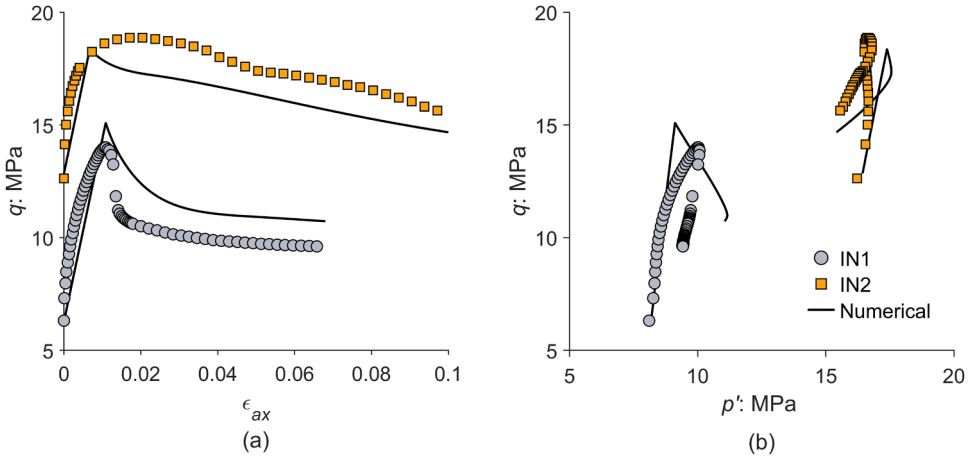

Fig. 2. Comparison between model predictions and experimental data for the intact Santerno Clay in undrained triaxial tests: (a) deviatoric stress-strain curves; and (b) effective stress paths (experimental data after [81]).

rightward slope of the effective stress paths. This feature was captured by setting $\alpha = 0.83$; α was then used as an equivalent parameter to better reproduce the elasto-viscoplastic response before failure. For both specimens, it was assumed that the stress states corresponding to peak strength lie on the same initial yield surface (i.e. the one of the material in site). This was achieved through an accurate selection of model parameters and initial state variables characterising the yield surface and its initial size (α_y, β_y, α_t, p_c and b_0). The analysis of the post-peak response allowed considering that yielding takes place in the dilatant-softening region of the curve. Indeed, after the peak, it can be observed that the deviator of stress decreases (Fig. 2a). The pore water pressure decreases leading to an increase of the mean effective stress for specimen IN1, whereas the opposite trends are observed for specimen IN2 (Fig. 2b).

Tests on both Santerno and Opalinus clays revealed significant softening, which is often associated with strain localization and shear banding. However, the present study does not specifically address these phenomena, as the material behaviour is simulated at a single integration point. Consequently, while the model captures the post-peak responses qualitatively, the results at large strains should be interpreted with caution.

3. Viscosity effects on the cyclic response of caprocks

3.1. The role of viscosity in cyclic degradation

Cyclic loading is of interest in UGS, where natural gas is stored in depleted hydrocarbon reservoirs when energy demand is low and recovered when energy demand is high. Similar issues may also arise in the context of hydrogen storage projects, where depleted reservoirs are used to balance supply and demand cycles over seasonal and annual timescales caused by the intermittent nature of renewable energy.[3,51]

The alternation of injection and production stages may induce a complex stress path in the caprock, potentially compromising the integrity of the formation.[85] Indeed, experimental evidence has shown that structured geomaterials can undergo progressive degradation when subjected to cyclic loading, with inelastic strain accumulation and eventually brittle failure.[52,86–88]

The time evolution of a typical loading scenario of UGS can be approximately schematized in undrained triaxial tests as a sinusoidal one-way deviatoric loading applied around a mean deviatoric stress q_{mean} with an amplitude A, corresponding to a maximum stress $q_{\max} = q_{mean} + A$. In the caprock, $q_{\max}$ is related to the maximum amount of gas to be stored, while A is associated with reservoir pressure declines needed to balance energy supply and demand cycles. Fig. 3 shows the results of three cyclic undrained triaxial tests carried out at the geotechnical Laboratory of the Politecnico di Torino on intact specimens of Santerno Clay in terms of stress-strain response (data from [89]). The specimens were anisotropically consolidated up to the in-situ stress state, namely: $q = 6.3$ MPa, $p' = 8.1$ MPa. A sinusoidal deviatoric loading with a time period $T = 5$ min was subsequently applied up to failure, adopting $q_{\max} = 12.5$ MPa and three different values of A, namely: 5.25 MPa, 4.25 MPa, and 3.25 MPa, which corresponds to $q_{mean} = 7.25$ MPa, 8.25 MPa, and 9.25 MPa, respectively. Upon application of a certain number of loading cycles N_f, a progressive degradation of the material structure is observed, resulting in a sudden, brittle failure in all the experimental tests. Additionally, it can be observed that a reduction in the value of A correlates with a reduction in the number of cycles to failure N_f.

The ability to capture the dependency of the number of cycles to failure N_f from the cyclic loading characteristics is probably the most important aspect for the assessment of caprock integrity in UGS projects. As shown in the previous section, material degradation is usually modelled via a damage variable that evolves with the plastic strain increment, both volumetric and deviatoric: to reproduce destructuration under cyclic loading it is therefore necessary to predict inelastic strains even within the yield surface. This is the case for constitutive models developed within the framework of bounding surface plasticity. For instance, Seidalinov and Taiebat[40] presented the SANICLAY-B, an improved version of the SANICLAY (Simple ANIsotropic CLAY plasticity, after [90]) developed to capture the behaviour of natural and remoulded anisotropic clays under monotonic and cyclic loading. The model employs a non-associative flow rule, and both the bounding surface and the plastic potential can undergo isotropic and rotational hardening. The plastic modulus is defined as a function of a shape-hardening parameter that evolves with the increase of plastic deviatoric strains, simulating the evolution of stress-strain loops and the consequent stiffness degradation during cyclic loading. In addition, an isotropic degradation mechanism is used to simulate destructuration.[33] When cyclic loading is applied under stress control, fragile failure may eventually occur, depending on the characteristics of the loading.

As an example related to applications to shallow formations, Fig. 4 reports the dependence of the number of cycles to failure N_f on the loading amplitude A for two sensitive marine clays, the Ariake and the Cloverdale clays, as simulated by the SANICLAY-B model. The cyclic responses were predicted according to the constitutive parameters and the initial state variables calibrated by Seidalinov and Taiebat[40] and Palmieri and Taiebat,[41] respectively for the Cloverdale and the Ariake clays. The simulations refer to specimens isotropically consolidated up to $p'_0 = 200kPa$ and then subjected, under undrained conditions, to sinusoidal one-way loadings with $q_{\max} = 100kPa$. The trends in Fig. 4 obtained with the SANICLAY-B are in contrast with the experimental results for the intact Santerno Clay. For loading protocols characterized by a fixed $q_{\max}$, the model predicts that the larger A, the larger, the smaller the number of cycles to failure N_f. This is due to the increase with A of the plastic modulus degradation and of mechanical destructuration. In turn, the experimental relationship between A and N_f is reversed for the intact Santerno Clay (Fig. 3).

Such opposite trend could be explained by accounting for the time-dependent behaviour of structured clays and clayrocks.[52,54,55,66,67] Under monotonic strain-controlled conditions, the peak shear strength q_{peak} depends on the strain-rate, while the critical state appears to be independent of rate effects.[54,55,81] Therefore, the response to cyclic loadings is also expected to depend on the rate of application of loading or, equivalently, the period, as observed mainly in experimental studies on structured clays[52,91] (see also the next section, where the comparison between two tests characterised by the same loading protocol, but with different periods, is presented). It is also well-known that the creep strain, or its dual strain-rate dependence, increases with the applied stress. Especially at very large periods, such as those used in the tests shown in Fig. 3, the response of a structured clay under a one-way cyclic loading is thus expected to be the result of two different mechanisms operating simultaneously. On the one hand, the continuous load reversal induces a progressive cyclic degradation of the mechanical response, which is faster the larger the loading amplitude A.[86–88] On the other hand, the application of some loading cycles lasts for a certain time during which a deviatoric stress, with a mean value equal to q_{mean}, is applied to the material. Thus, the persistence of the loading implies the development of viscous strains, which typically are larger the larger is q_{mean}. The two mechanisms work together to accumulate inelastic strains, leading to progressive destructuration and ultimately fragile failure.[89] For tests performed with the same $q_{\max}$, the loading amplitude has an opposite influence on the two mechanisms, since larger A implies both larger cyclic degradation and smaller viscous strains because of the reduction in q_{mean}. The experimental results in Fig. 3 for the intact Santerno Clay suggest that, for the caprock material and loading histories here considered, the viscous mechanism is somehow prevailing.

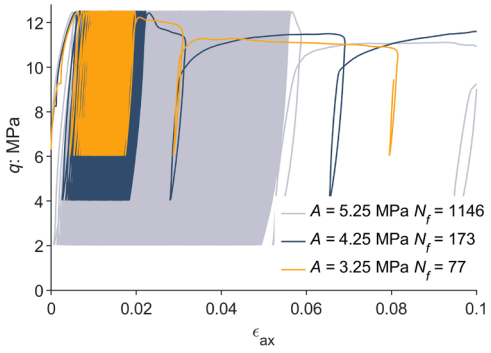

Fig. 3. Experimental results of undrained cyclic triaxial tests carried out on intact Santerno Clay imposing a sinusoidal deviatoric loading with $T = 5$ min, $q_{\max} = 12.5$ MPa and different amplitudes A (data from [89]).

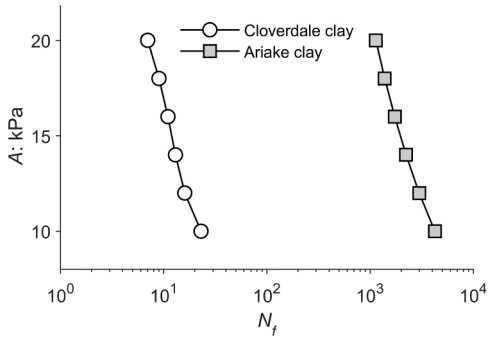

Fig. 4. Dependency of N_f from A for two structured clayey materials isotropically consolidated up to $p'_0 = 200kPa$ and then subjected to sinusoidal loadings with $q_{\max} = 100kPa$. Calibration parameters from Seidalinov and Taiebat[40] and Palmieri and Taiebat,[41] respectively for the Cloverdale and the Ariake clays.

This cannot be reproduced with inviscid bounding surface plasticity.

To account for both degradation mechanisms, a viscoplastic extension of the Gens and Nova[29] framework is proposed in the following. Viscoplastic strains are modelled in light of the extended overstress theory,[63,92] which can capture creep and strain rate effects occurring also within the yield surface. It should be noted that this choice is crucial for modelling the counterintuitive trends presented in Fig. 3. Indeed, for cyclic loads characterised by the same q_{max}, an increase in the applied q_{mean} will imply an increase in the inelastic strain accumulation and, in turn, a larger cyclic destructuration.

The proposed constitutive framework is intended to be a relatively simple, albeit effective, frame to simulate the main trends observed in the fatigue life of caprocks subjected to cyclic loadings, as it neglects aspects of the cyclic response of soils (e.g. the smooth transition from the practically linear to the highly nonlinear regime) that are crucial for other applications, such as seismic or offshore engineering.

3.2. Elasto-viscoplastic constitutive framework

With the introduction of viscosity into the elasto-plastic framework, the strain-rate tensor $\dot{\varepsilon}$ can be decomposed as:

$$\dot{\varepsilon}_{ij} = \dot{\varepsilon}^{e}_{ij} + \dot{\varepsilon}^{vp}_{ij} \tag{22}$$

where $\dot{\varepsilon}^{vp}_{ij}$ is the viscoplastic component. Note that the dot notation is used to denote the derivative with respect to time, i.e. the rate of a certain variable, where time plays a physical role.

The elastic behaviour is assumed to be consistent with the elasto-plastic model introduced in Section 2.2. The viscoplastic response is instead obtained as in Vermeer and Neher,[93] according to the extended overstress theory (see also [69,70]), where the static yield surface typical of the overstress theory[63,92] is replaced by a reference surface f_r.

The model formulation is based on the observation that when a normally consolidated soil is loaded under isotropic conditions, after pore pressure dissipation, the viscoplastic volumetric strain ε^{vp}_{vol} increases linearly with the logarithm of time. Consequently, the viscous parameter μ^* can be defined as:

$$\mu^* = \frac{\varepsilon^{vp}_{vol} - \overline{\varepsilon}_{vol}{}^{vp}}{\ln\left(\frac{t}{\tau}\right)} \tag{23}$$

being $\overline{\varepsilon}^{vp}_{v}$ the viscoplastic volumetric strain developing at a reference time $\tau = 24$ hours.

According to the extended overstress theory, a reference surface f_r is associated with a material which has been loaded for a time τ. The dynamic loading surface f_d instead describes the current stress-state. The two surfaces are here assumed to have the same formulation of the yield surface adopted for the elasto-plastic framework (Eq. 11). In Eq. 11 p_{cb} is now replaced by p^r_{cb} and p^d_{cb}, while p_t is replaced by p^r_t and p^d_t, respectively for f_r and f_d. The role of material structure is again modelled as in Eq. 13 and Eq. 14.

As far as the yield surface in the elasto-plastic framework, f_r and f_d evolve with the accumulation of inelastic strains due to both plastic hardening of remoulded material and degradation. The viscoplastic model follows the same hardening and damage laws presented in Eq. 7 and Eq. 15, where viscoplastic strain increments are used in lieu of plastic increments.

In compliance with the Vermeer and Neher[93] model, the full viscoplastic strain-rate tensor $\dot{\boldsymbol{\varepsilon}}^{\boldsymbol{vp}}$ can be computed according to the following flow rule:

$$\dot{\boldsymbol{\varepsilon}}^{\boldsymbol{vp}} = \frac{1}{\alpha_{VN}} \frac{\mu^*}{\tau} \left(\frac{p^d_{cb} + p^d_t}{p^r_{cb} + p^r_t}\right)^{\frac{\lambda^* - \kappa^*}{\mu^*}} \frac{\partial g}{\partial \boldsymbol{\sigma}'} \tag{24}$$

where: $\lambda^* = \frac{\lambda}{1+e_0}$; $\kappa^* = \frac{\kappa}{1+e_0}$; $\boldsymbol{\sigma}'$ is the effective stress tensor; g is the plastic potential as defined in Eq. 12; and $\alpha_{VN} = abs\left(\frac{\partial g}{\partial p'}\right)$ is a normalization factor that ensures that the viscoplastic volumetric strain-rate under isotropic conditions is equal to:

$$\dot{\varepsilon}^{vp}_{vol} = \frac{\mu^*}{\tau} \left(\frac{p^d_{cb} + p^d_t}{p^r_{cb} + p^r_t}\right)^{\frac{\lambda^* - \kappa^*}{\mu^*}} \tag{25}$$

3.3. Model Calibration

The capabilities of the elasto-viscoplastic model are validated in the next section against experimental data obtained from cyclic triaxial tests performed on intact specimens of caprock from the Santerno Clay formation. The model requires the definition of just one additional parameter, the modified creep index μ^*, with respect to the elasto-plastic model described in Section 2.2. As highlighted by Vermeer and Neher,[93] μ^* is defined as the slope of the volumetric strain plotted against the logarithm of time, developing after a stepwise increase of axial load in a standard oedometer test in normally consolidated conditions. It should be noted that μ^* is defined here from a phenomenological point of view and it is beyond the scope of this paper to discuss the causes of the viscosity of geomaterials. However, it is worth mentioning that creep has often been explained in terms of chemical processes triggered by local mechanical damage,[94,95] which can break the chemo-mechanical bonds of the skeleton,[62] further suggesting that viscous strains contribute to the damage of the material. By following the same conceptual approach employed by Gens and Nova,[29] this parameter is assumed to be independent of the material structure. Therefore, its value was calibrated by referring to the results of oedometer tests carried out on remoulded material.

Fig. 5 presents the comparison between experimental data and model prediction for the oedometric response of remoulded Santerno Clay specimens. The numerical simulations were obtained by defining the viscosity parameter $\mu^* = 0.0034$ as stated above, and keeping the other model parameters as in Table 1. During the remoulding procedure, the slurry underwent preliminary consolidation under one-dimensional conditions up to an effective vertical stress σ_v' equal to about 9.3 MPa. This value was therefore used to compute the corresponding $p^d_c = 9$ MPa, being $b = 0$.

Fig. 5a shows the good prediction of the constitutive model in terms of the compression curve up to large effective vertical stresses. The time evolution of the axial strain is presented in Fig. 5b for some selected stepwise increases in loading. In the numerical simulations, the primary consolidation was roughly approximated by referring to Terzaghi's one-dimensional consolidation theory.[96] Most of the steps were carried out for a standard time of about 24 hours, except for the one corresponding to an increase from 14 MPa to 28 MPa where the load was kept constant for 6 days to clearly observe the evolution of the creep strains and the following hardening. With the adopted value of μ^*, the model can capture the observed viscous response for a wide range of σ_v' values, corresponding to both normal and overconsolidated states of the material.

Once μ^* was calibrated, it was necessary to slightly adjust the parameters previously identified for modelling the response of the intact material. It should be noted that in an elasto-viscoplastic model formulated based on extended overstress theory, the initial value of the hardening parameter $p^r_{cb,0}$ does not only depend on the maximum consolidation stress applied to the material in the history, but also on the reference time τ.[9,93] To obtain the same predictions as in the elasto-plastic model for undrained monotonic triaxial tests conducted at an axial strain-rate of 0.01 %/min (Fig. 2), it was therefore necessary to adopt a different value for $p^r_{cb,0}$ with respect to the value of $p_{cb,0}$. This was taken in account by reducing b_o and, consequently, slightly adjusting the values adopted for h_{dev} and h_{vol}. The other model parameters were instead kept equal to the elasto-plastic model. The constitutive parameters and the initial internal variables calibrated to simulate the

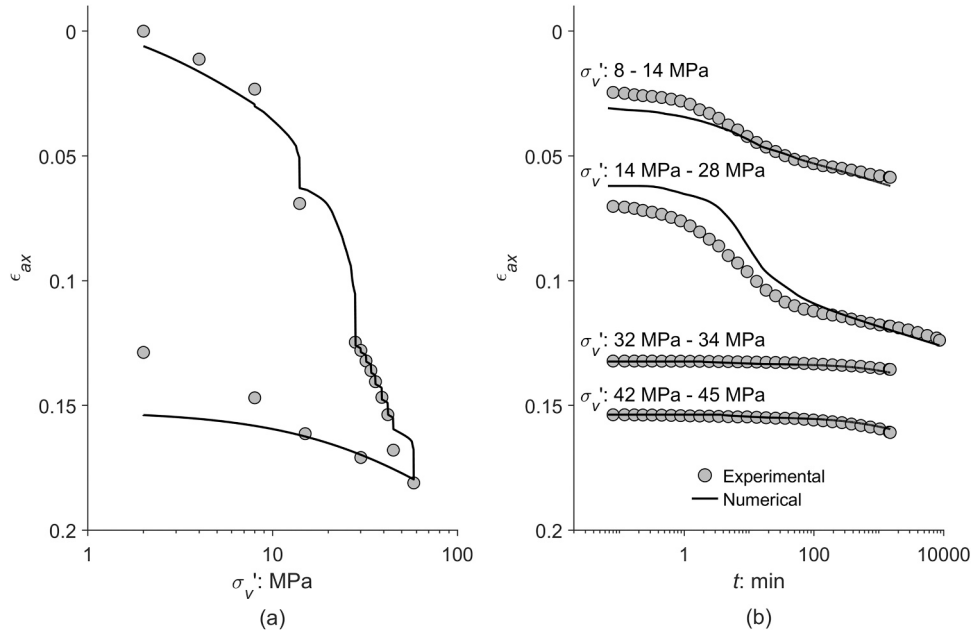

Fig. 5. Comparison between model predictions and experimental data of the oedometric response of remoulded Santerno Clay: (a) compression curve; (b) evolution of axial strain with time.

response of the intact material are presented in Table 2.

The extension to viscoplasticity allowed the strain-rate dependence of peak strength to be captured without ad hoc 'tuning' of the model parameters. Fig. 6 compares numerical simulations and experimental results of the peak deviatoric stresses q_{peak} as a function of the imposed axial strain-rate $\dot{\varepsilon}_{ax}$. The data refer to intact caprock specimens anisotropically consolidated up to $p' = 8.1$ MPa and $q = 6.3$ MPa and then sheared under undrained conditions (experimental results from [81]). The model predictions are in excellent agreement with the experimental results in the range of $\dot{\varepsilon}_{ax}$ between 0.01 %/min and 0.5 %/min, while the peak strength at a lower strain-rate is slightly underpredicted. Nevertheless, the comparison was considered to be satisfactory for the simulation of the cyclic tests discussed in the following section.

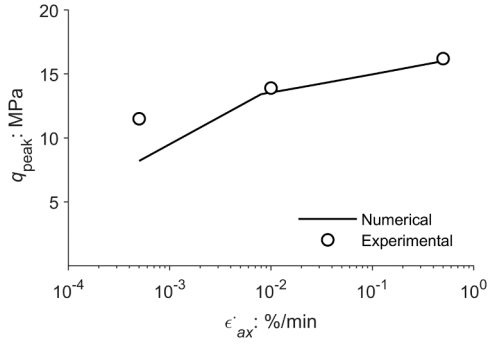

Fig. 6. Comparison between model predictions and experimental data of the peak strength of intact Santerno Clay from undrained triaxial tests at different strain-rates (experimental data after [81]).

3.4. Numerical simulations of the fatigue behaviour

The model is validated against experimental results of undrained cyclic triaxial tests performed by Ciancimino et al.[81] and Ciancimino et al.[89] The caprock was firstly consolidated up to $p' = 8.1$ MPa and $q = 6.3$ MPa. The deviator was then monotonically increased under undrained conditions up to q_{mean} before applying a sinusoidal one-way loading up to failure. Most of the tests here considered were carried out adopting a period of 5 min, except for one test which was carried out with $T = 250$ min. However, cyclic loadings applied under stress control will lead to variable strain rates. As a reference value, an average strain rate $\bar{\dot{\varepsilon}}_{ax,c}$ for each test can be computed as:

$$\bar{\dot{\varepsilon}}_{ax,c} = \frac{4\bar{\varepsilon}_{ax,c}}{T} \tag{26}$$

being $\bar{\varepsilon}_{ax,c}$ the average axial strain applied during a quarter of the cyclic loading. The resulting value of $\bar{\dot{\varepsilon}}_{ax,c}$ is different from test to test due to the nonlinearity in the stress-strain response of the material, even if the loading is characterised by the same period. A summary of the experimental tests used as a benchmark is presented in Table 3, which reports the information on the imposed deviatoric loading history and the number of cycles to failure N_f.

Fig. 7 shows the comparison between numerical simulation and experimental data for test C-TX 06. The model predicts reasonably well the accumulation of inelastic strain shown by the experimental test (Fig. 7a). Such accumulation leads to progressive damage, which reduces the initial degree b_0 and the hardening variable p^r_{cb} and, in turn, increases the viscoplastic strain-rate cycle by cycle. Similar to what it was observed in the experimental tests, cyclic failure eventually occurs

Table 2
Model parameters and initial values of the internal variables used in the simulations of the undrained triaxial tests on intact Santerno Clay with the elasto-viscoplastic model.

κ	G	α	λ	μ*	M	α_y	β_y	p^r_{c0}	b_0	h_0	α_t	h_{dev}	h_{vol}
(-)	(MPa)	(-)	(-)	(-)	(-)	(-)	(-)	(MPa)	(-)	(-)	(-)	(-)	(-)
0.033	300	0.83	0.102	0.0034	1	0.62	1.1	13.5	0.47	0	0	20	250

Table 3
Summary of the anisotropically consolidated undrained cyclic triaxial tests on intact Santerno Clay (experimental data from Ciancimino et al.[81] and Ciancimino et al.,[89] the IDs refer to the original ones reported in the papers).

ID	q_{max}: MPa	A: MPa	q_{mean}: MPa	T: min	N_f	$\bar{\dot{\varepsilon}}_{ax,c}$: %/min
C-TX 01	13	3.25	9.75	5	18	0.18
C-TX 04	13	5.25	7.75	250	7	0.004
C-TX 05	13	5.25	7.75	5	60	0.19
C-TX 06	13.5	5.95	7.55	5	13	0.33
C-TX 07	12.5	5.25	7.25	5	1146	0.27
C-TX 08	12.5	3.25	9.25	5	77	0.10
C-TX 09	12.5	4.25	8.25	5	173	0.16

after a certain number of loading cycles N_f. It is interesting to note that, for a model formulated within the framework of the extended overstress theory, the concept of cyclic failure under stress control is associated with the development of very large strain-rates, rather than with the attainment of certain failure stress. Unlike classical elasto-plasticity, in elasto-viscoplasticity it is theoretically always possible to reach a certain deviator (e.g. the q_{max} value of the cyclic loading histories), but possibly at the price of developing extremely large viscoplastic strain-rates. The simulated stress paths are in good agreement with the experimental data (Fig. 7b), especially concerning the slope of the cycles which is mainly defined by the assumed cross-anisotropic elasticity. As also shown by the simulations of the monotonic response of the intact caprock (Fig. 2), the progressive destructuration is accompanied by the development of slightly too large negative excess pore pressures with respect to the experimental data. The simulated cyclic stress path therefore tends to move to the right as the cyclic failure is approached. An aspect of the observed response that is not well captured by the model is the non-linear behaviour shown in the stress-strain cycles even at very low strains (Fig. 7a), as anticipated by the dependence of the entity of the viscoplastic strain-rate on the ratio $(p^d_{cb}+p^d_t)/(p^r_{cb}+p^r_t)$ (see Eq. 24). It is therefore not possible to model a sufficiently smoothed transition from the practically linear (at very small strains) to the highly nonlinear regime.

The comparison between model predicted and experimental number of cycles to failure is shown in Fig. 8. The performance of the model is assessed based on three scenarios corresponding to different deviatoric loading histories: (*i*) same $A = 5.25$ MPa and $q_{max} = 13$ MPa, varying T; (*ii*) same $T = 5$ min and $A = 5.25 \div 5.95$ MPa, varying q_{max}; and (*iii*) same $T = 5$ min and $q_{max} = 12.5$ MPa, varying A.

The same sinusoidal deviatoric load applied with different periods leads to significantly different strain-rates. In virtue of the role played by viscosity, progressive destructuration will occur at a smaller number of cycles as T increases. The proposed model seems able to reproduce the influence of T on N_f, as shown in Fig. 8a. The larger the q_{max}, the larger the accumulation of inelastic strains and hence the destructuration. The N_f therefore tends to decrease as q_{max} increases, as shown by the experimental results in Fig. 8b, which were carried out adopting about the same T and similar A values. Note that for tests conducted using the same A, an increase of q_{max} also implies an increase of q_{mean}. As a result, cyclic destructuration increases significantly, as the viscous strain development is typically greater as q_{mean} increases and the stress paths approach the yield surface. This can be clearly seen by comparing the results of tests carried out using the same A, e.g. tests C-TX 05 and 07. The trend is satisfactorily reproduced by the model, for which an increase in q_{max} implies larger $(p^d_{cb}+p^d_t)/(p^r_{cb}+p^r_t)$ values and, in turn, larger viscoplastic strain-rates (see Eq. 24).

Finally, Fig. 8c compares experimental and numerical results in terms of N_f as a function of A. The introduction of viscosity allows the counterintuitive trends in Fig. 3 to be partially reproduced. The model predicts indeed an increase in N_f with increasing A, although the influence of A is more pronounced in the experimental tests.

The numerical simulations shown in Fig. 7 and Fig. 8 are in good agreement with the experimental data. Of course, model predictions could be further improved by introducing more sophisticated approaches to modelling material behaviour within the reference surface, such as models formulated within the bounding surface framework but with the introduction of viscosity.[97,98] However, this would significantly increase the complexity of the model possibly reducing its applicability to large-scale problems (such as UGS applications), for which capturing the general trends of N_f is probably the most relevant aspect.

4. Introduction of chemical degradation for the interaction between caprock materials and CO_2

4.1. The role of chemical degradation in carbon capture and storage activities

Geological storage of CO_2 is one of the measures proposed to contain climate change. CO_2 is collected from the sites where it is produced and then injected in reservoirs, in liquid or dry supercritical state (pressure above 7.4 MPa and temperature above 31 °C). The difference between the pressure of injected CO_2 in the reservoir and the pore pressure of the caprock must be kept below its threshold capillary pressure. This ensures that immiscible CO_2 is contained in the reservoir. Nevertheless, transport and geochemical processes are expected to occur because of the solubility of CO_2, as part of it dissolves in the brine and the solute is transported through the caprock. Dissolution of CO_2 causes brine

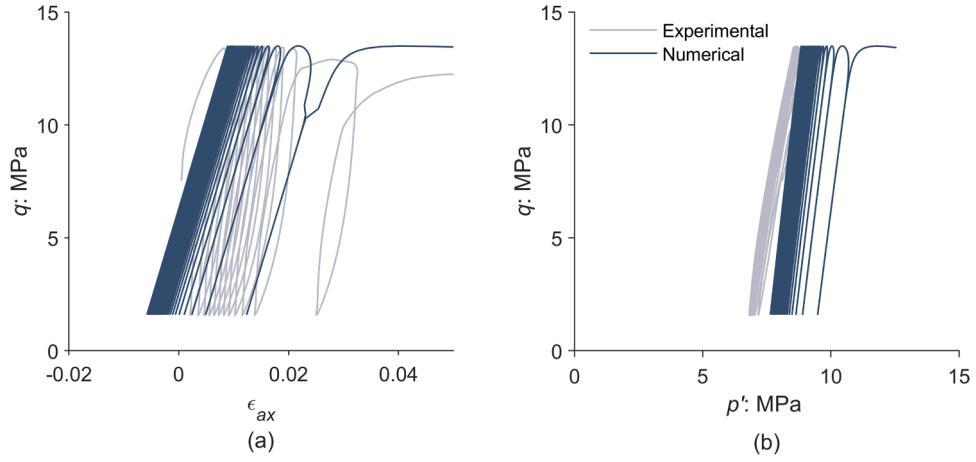

Fig. 7. Comparison between model predictions and experimental data for intact Santerno Clay in the undrained cyclic triaxial test C-TX 06: (a) deviatoric stress-strain curves; and (b) effective stress paths (data from [89]).

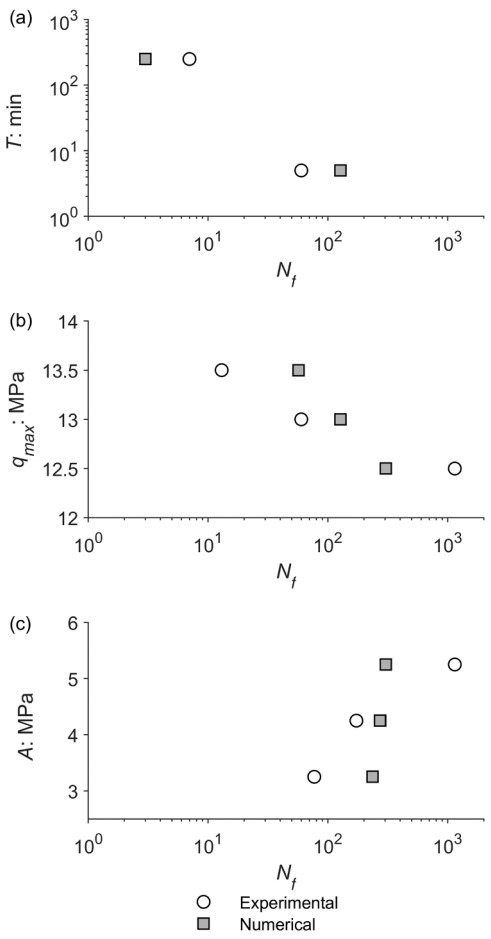

Fig. 8. Comparison between model predictions and experimental data for intact Santerno Clay in undrained cyclic triaxial tests in terms of number of cycles to failure as a function of: (a) loading period, tests C-TX 4 and 5; (b) maximum deviator, tests C-TX 5, 6, and 7; (c) amplitude, tests C-TX 7, 8, and 9.

acidification (increase of H^+, i.e. decrease of pH), which occurs according to the following reaction pathway:

a. $CO_2 + H_2O \rightleftharpoons H_2CO_3^*$ (27)

b. $H_2CO_3^* \rightleftharpoons H^+ + HCO_3^-$

c. $HCO_3^- \rightleftharpoons H^+ + CO_3^{2-}$

Brine acidity may trigger geochemical reactions that induce the dissolution of certain minerals constituting the caprock, with anticipated effects not only on the caprock permeability and porosity but also on its mechanical behaviour (see, e.g., the extensive reviews [19,99]). The attention is here focused on the description of a constitutive framework to reproduce such effects, bearing in mind that both experimental data[100] and numerical geochemical simulations[101] on caprock materials have highlighted that the most immediate attack of the acidified brine is mostly on the carbonate minerals, due to their fast reaction kinetics. In the long term, vice versa, the acidified brine can also react with the alumino-silicate minerals (i.e. feldspars and clays) present in the caprock. However, such reactions may occur over periods of tens, hundreds or thousands of years due to the slow reaction kinetics of these minerals.

Within this context, one of the advantages of the elasto-plastic strain-hardening model described in Section 2 is that it can be easily extended to include material degradation induced by chemical reactions, as suggested, for instance, by Nova et al.,[30] Gajo et al.,[35] and Ciantia and di Prisco.[58] To account for the chemical degradation induced by pore water acidification, the internal variables can be modified by including the effect on material degradation caused by rock-water-CO_2 interaction, both in terms of strength and stiffness. The effects of chemical degradation can then be simulated through the introduction of a new variable, i.e. the specific material dissolved mass m_b, defined as the ratio between the dissolved material mass and the total solid components mass. This variable provides the coupling between the mechanical behaviour of the material and the geochemical reactions acting in the pore fluid induced by its acidification.

In this section, the suitability of the mechanical framework depicted in Section 2 for structured soils and soft rocks to account for CO_2-induced caprock degradation is investigated. In particular, the chemical input to the mechanical model is provided by the dissolved mineral mass obtained by a numerical reactive transport model, implemented in the FEM code Comsol Multiphysics. To keep the geochemical scenario as simple as possible, and in consideration of the time frame typically employed in mechanical laboratory testing in engineering practice (certainly smaller than that required to measure any appreciable dissolution of alumino-silicate minerals), material degradation is evaluated only concerning the carbonate solid components, in particular calcite.

4.2. *Extension of the elasto-plastic constitutive framework to account for chemical degradation*

The role of the chemical degradation is introduced in the elasto-plastic framework via the damage variable h, whose evolution is set to depend not only on the plastic strain increment (as in Eq. 16), but also on the chemical dissolution of the solid mass, as:

$$\mathrm{d}h = h_{dev}\left|\mathrm{d}\varepsilon^p_{dev}\right| + h_{vol}\left|\mathrm{d}\varepsilon^p_{vol}\right| + h_{chem}\mathrm{d}m_b \tag{28}$$

where the parameter h_{chem} controls the dependency of the damage variable h on the dissolved mass evolution $\mathrm{d}m_b$, which in turn is an output of geochemical analyses. The model relies on the assumption that the variable b can also be used to reproduce the mechanical effects induced by chemical degradation (as induced by mineral dissolution) so that Eq. 15 can still be used.

According to Gajo et al.,[35] the dependency of the elastic properties on the mechanical and chemical degradation can be introduced by specifying an appropriate elastic free energy density function, within the context of hyperelasticity and elasto-plastic coupling, leading to equivalent elastic moduli. In their original model, this stems from the assumption that the macroscopic elastic free energy can be written as the linear interpolation between the free energy of a cementation-free configuration and the one of the completely cemented configuration. For consistency with the adopted framework, the equivalent elastic modulus of the structured material E is set to depend on both the elastic modulus of the natural material E_b (assumed to correspond to the modulus of the completely structured soil) and of the one of the degraded material, E_g:

$$E = E_g\left(1 - a_b^{\alpha_d}\right) + E_b a_b^{\alpha_d} \tag{29}$$

where α_d is a material parameter. In the original framework, a_b is conceived as a normalized structure degree:

$$a_b = \frac{b}{b_0} \tag{30}$$

Equivalent bulk K and shear G moduli can be defined as:

$$K = K_g\left(1 - a_b^{\alpha_d}\right) + K_b a_b^{\alpha_d} \tag{31}$$

$$G = G_g\left(1 - a_b^{\alpha_d}\right) + G_b a_b^{\alpha_d} \tag{32}$$

As assumed by Gajo et al.,[34] the elastic volumetric strain increment is then expressed as a sum of two contributions, the one induced by

mechanical loading, $d\varepsilon_{vol}^{e,mec}$, and the one induced by the chemical dissolution, $d\varepsilon_{vol}^{e,chem}$, as:

$$d\varepsilon_{vol}^{e} = d\varepsilon_{vol}^{e,mec} + d\varepsilon_{vol}^{e,chem} \tag{33}$$

The elastic volumetric strain induced by chemical dissolution can be simply evaluated as:

$$d\varepsilon_{vol}^{e,chem} = \kappa_{chem} dm_b \tag{34}$$

where κ_{chem} is a non-dimensional parameter. As for the elastic deviatoric strain induced by chemical dissolution, its contribution is considered negligible:

$$d\varepsilon_{dev}^{e,chem} = 0 \tag{35}$$

The remaining part of the model can be kept as described in Section 2. It is worth noting that, as long as b changes according to chemical degradation, the size of the yield surface is expected to decrease with pore fluid acidification, with consequences on the predicted strength.

4.3. Bridging the gap between mechanical and geochemical models: estimate of the dissolved solid mass m_b

The constitutive framework is here applied to reproduce the mechanical effects induced on caprocks by carbonate dissolution. To bridge the gap between geochemical analyses and mechanical constitutive modelling, the calcite mass fraction variation is evaluated according to a FEM geochemical model, in order to provide a sound physical basis for the chemical variable introduced in the mechanical model. The model includes the water mass balance equation for the saturated porous medium and the mass balance equation for all the primary species dissolved in water, according to the theoretical approach presented in Steefel and Lasaga.[102] The proposed modelling approach accounts for both the aqueous (homogeneous) reactions of CO_2 dissolved in water (assumed to be in equilibrium) and the dissolution kinetics of calcite in the acidic environment induced by CO_2 injection.

Finally, calcite dissolution is linked to porosity changes via the reactive surface area of the mineral and the reaction rate. Chemo-hydraulic coupling is addressed by considering porosity changes in the storage term of the balance equations and by introducing a suitable link between hydraulic conductivity and current porosity. The model requires the solution of an initial chemical speciation problem, which was carried out using the PHREEQ-C software, and then the integration of a set of partial differential equations (the mass balance equations of water and of the main primary species dissolved in water) and non-linear algebraic equations (to obtain the concentration of all the chemical species involved). In this study, this was done using the finite element software Comsol Multiphysics, following the approach presented by López-Vizcaíno et al.[103] Calcite dissolution is described via the following reaction pathway:[104]

a. $CaCO_3 + H^+ \rightleftharpoons Ca^{2+} + HCO_3^-$ (36)

b. $CaCO_3 + H_2CO_3^* \rightleftharpoons Ca^{2+} + 2HCO_3^-$

c. $CaCO_3 \rightleftharpoons Ca^{2+} + CO_3^{2-}$

while the rate of calcite dissolution can be estimated via the transition state theory,[105,106] as:

$$r_{CaCO_3} = \left(k^{acid} a_{H^+} + k^{neutral} + k^{carb} a_{H_2CO_3^*}\right)\left(1 - \frac{a_{Ca^{2+}} a_{CO_3^{2-}}}{K_{eq,calc}}\right) \tag{37}$$

where k^{acid}, $k^{neutral}$, k^{carb} $\left(\frac{mol}{m^2 s}\right)$ are empirical specific dissolution rates which depend on temperature, and $K_{eq,calc}$ is the equilibrium constant of calcite dissolution in water ($K_{eq,calc} = 10^{-8.49}$). The rate of change in volume fraction of calcite is therefore evaluated as:

$$\dot{\phi}_{CaCO_3} = -r_{CaCO_3} \cdot S_{CaCO_3} \cdot V_{m,CaCO_3} \cdot \phi_{CaCO_3} \tag{38}$$

where S_{CaCO_3} is the specific surface of calcite, $V_{m,CaCO_3}$ is the molar volume of calcite, and ϕ_{CaCO_3} is the calcite volumetric fraction. From Eq. 38, the change in porosity ϕ due to geochemical reactions can be obtained (in the hypothesis of negligible volumetric strain induced by the chemical reactions) as:

$$\phi = 1 - \phi_{non-reac} - \phi_{CaCO_3} \tag{39}$$

where $\phi_{non-reac}$ is the volume fraction of the non-reactive grains. It is worth mentioning that Eq. 40 describes the total rate of reacting calcite dissolution, including both the positive (i.e. dissolving calcite) and the negative (reprecipitating calcite):

$$r_{CaCO_3} = r_{CaCO_3}^{diss} + r_{CaCO_3}^{prec} \tag{40}$$

with:

$$r_{CaCO_3}^{diss} = k^{acid} a_{H^+} + k^{neutral} + k^{carb} a_{H_2CO_3^*} \tag{41}$$

$$r_{CaCO_3}^{prec} = -\frac{a_{Ca^{2+}} a_{CO_3^{2-}}}{K_{eq,calc}}\left(k^{acid} a_{H^+} + k^{neutral} + k^{carb} a_{H_2CO_3^*}\right) \tag{42}$$

In the following, it is assumed that the mechanical effect is relevant just in terms of the dissolution of calcite in its original form and that, in the short term, reprecipitated calcite has a negligible mechanical effect. Thus, the dissolved original calcite mass $\phi_{CaCO_3,b}$ can be estimated by integrating in time the expression:

$$\dot{\phi}_{CaCO_3} = -r_{CaCO_3}^{diss} \cdot S_{CaCO_3} \cdot V_{m,CaCO_3} \cdot \phi_{CaCO_3} \tag{43}$$

The geochemical variable required by the mechanical model is then:

$$\dot{m}_b = \rho_{s,calc} \dot{\phi}_{CaCO_3} \tag{44}$$

4.4. Numerical simulation of experimental tests

The FEM model was used to reproduce the experimental data reported by Lyu et al.[107] on Longmaxi Shale specimens subjected to CO_2 exposure for different time intervals before uniaxial compression tests. Samples were extracted from a slightly weathered outcrop of Longmaxi Shale in Sichuan Basin (China), which, thanks to its good mechanical properties and low permeability, has been selected as a suitable caprock for CO_2 geological sequestration. Cylindrical specimens with initial calcite mass fraction $m_{b0} = 4.4$ % and porosity $\phi_0 = 0.272$ were prepared with a diameter of 30 mm and height of 60 mm. The specimens were soaked in a high-pressure chamber for 10, 20 or 30 days, being immersed in NaCl brine (NaCl mass concentration equal to 20 %) in contact with either liquid (pressure 7 MPa) or supercritical (pressure 9 MPa) CO_2. Subsequently, the specimens were taken out and left in the laboratory environment for 24 hours to ensure pore pressure dissipation. Finally, uniaxial compression tests were carried out imposing a strain-rate of 0.17 %/min.

The shale is composed of approximately 55 % (by mass) quartz and 15 % feldspar, with a total clay content of less than 6 % and a calcite fraction of 4.4 %. According to the Authors' interpretation (also presented in other papers [108]), the observed change in the mechanical properties of the shale (both strength and stiffness) is related to the physical and chemical reactions that occur during imbibition. In general, the increasing acidity of the pore fluid could lead to the dissolution and precipitation of several minerals (including K-feldspar, carbonates, some clay minerals and iron-bearing minerals), which in turn create pores and enlarge cracks, reducing the strength and stiffness of the shale. Here, the change in mechanical properties was related to calcite dissolution due to the much higher dissolution rate of carbonates compared

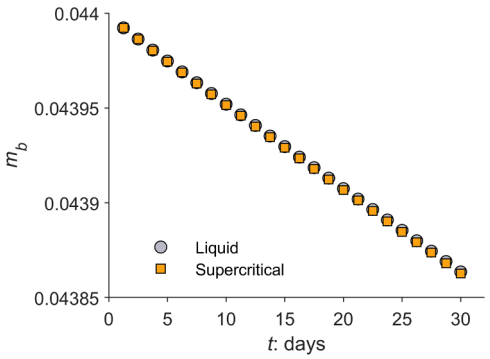

Fig. 9. Numerical predictions of the evolution in time of the calcite mass fraction m_b for specimens exposed to liquid and supercritical CO_2 (experiments from [107]).

to the other minerals in the Longmaxi Shale (see, e.g., [109]), and also to the imbibition time used in the experiments. From an experimental point of view, the stress-strain curves highlighted a reduction in compressive strength and shear stiffness that was inversely proportional to exposure time.

According to model predictions, geochemical reactions between the CO_2-saturated brine and solid minerals induced a progressive dissolution of calcite. The material dissolved mass $\Delta m_b(t) = m_{b0} - m_b(t)$ was quantified through a geochemical analysis performed with the finite element code described in Section 4.3 (see [103,110–112] for the finite element formulation). The reactive transport model was set up to mimic the experimental conditions, simulating the ageing of the samples saturated with brine in equilibrium with CO_2 in the high-pressure chamber. Two simulations were run to reproduce the liquid and supercritical CO_2 exposure. Model boundary conditions were imposed in terms of H^+ ion concentrations, which were evaluated based on Eq. 27. The related dissolved CO_2 concentrations were determined according to Henry's law, which states the proportionality between the solute concentration and the pressure of the fluid. The CO_2 pressure was 7 MPa for the liquid CO_2 and 9 MPa for the supercritical CO_2, leading respectively to H^+ concentrations equal to 1.0503 mol/m^3 and 1.194 mol/m^3. The transport of the dissolved species through the specimens was modelled by diffusion, having assumed a diffusion coefficient of $1.02 \cdot 10^{-8}$ m^2/s.[113]

The predicted evolution with time of the average (for the specimen) value of m_b is shown in Fig. 9 for the two numerical simulations. Remarkably, the numerical simulations also show (in agreement with the experimental evidence) that, since gaseous and supercritical CO_2 have similar solubilities in water, the samples subjected to soaking with gaseous and supercritical CO_2 have similar dissolution. The similar mechanical effects are a consequence of the same geochemical response.

The mechanical response of the Longmaxi Shale upon uniaxial compression loading was predicted with the constitutive model described in Section 4.2 adopting the parameters reported in Table 4. Chemical degradation was reproduced by letting the variable b evolve with m_b (obtained from the geochemical analyses) according with Eq. 15 and Eq. 28. Table 5 presents the m_b values at times of interest for the shearing phase. The results of the mechanical simulations are presented in Fig. 10.

It can be appreciated that, upon 30 days of exposure, the strength of the Longmaxi Shale reduces drastically to about half of its initial value. A very good reproduction of the experimental results was obtained by relating the variable b to the calcite mass fraction: the framework can indeed adequately simulate the reduction of the peak strength due to the shrinkage of the yield surface. By introducing the elasto-plastic coupling, it also models the reduction in the shear modulus caused by the dissolution of CO_2 in the pore fluid. Remarkably, just one single set of parameters was used for the whole set of simulations.

Table 5
Calcite mass fraction m_b and corresponding b values at times of mechanical tests.

Exposure time	m_b (-)	b (-)
0	0.044000	6.20
10 days	0.043934	4.39
20 days	0.043881	3.31
30 days	0.043837	2.69

5. Conclusions

Emerging applications in the geo-energy sector include CO_2 storage and UGS projects in deep aquifers and depleted reservoirs. The main signatures of such applications are the cyclic nature of the mechanical loads due to the seasonality of energy storage and production, and the chemical reactions that occur due to the geochemical interaction between the minerals forming the caprock and the stored fluids. All these processes induce complex chemo-hydro-mechanical paths, which are relatively slow in time and can lead to progressive degradation of the caprock behaviour.

Experimental evidence has shown the extreme fragility of carbonatic clays and shales, which can be effectively modelled with the elasto-plastic framework of Gens and Nova[29] by accounting for the role of material structure degradation. However, the applications described above require the framework to be extended to properly capture the time dependence of the mechanical response and/or its coupling with geochemical processes. In this study, the time dependence was accounted for by the explicit introduction of viscosity into the elasto-plastic framework through the extended overstress theory. Such an extension allowed, firstly, to correctly reproduce the strong dependence of the peak shear strength of an Italian stiff carbonatic clay on the strain rate, an aspect of great importance given the long timescales associated with reservoir applications. Time dependence and destructuration were also shown to control the cyclic response of the caprock material. Indeed, the application of stress-controlled cyclic loading can result in progressive destructuration and, after a certain number of loading cycles, fragile failure. The number of cycles to failure is strongly influenced by the amplitude and the period of the applied loading history. Both trends are satisfactorily captured by the extended model. In particular, the ability to model creep and strain-rate effects that also occur within the yield surface is a strict requirement to reproduce the increase in fatigue life with increasing cyclic amplitudes that has been experimentally observed for cyclic histories characterized by the same maximum deviator. Such a trend is in fact attributed to viscoplastic strains that develop at relatively low stresses (even within the elasto-plastic yield surface), associated with the persistence of the cyclic loading for a certain time. This aspect is particularly relevant for UGS studies, as injection/production operations in depleted reservoirs are characterised by very long periods (typically seasonal timescales), which are often incompatible with feasible test times in the laboratory. For such large periods, the viscous mechanism is likely to be even more

Table 4
Model parameters and initial values of the internal variables used in the simulations of the mechanical tests performed by Lyu et al.[107] on Longmaxi Shale.

$\kappa_b = \kappa_d$	G_b	G_d	α_d	α	λ	M	α_y	β_y	p_{c0}	b_0	h_0	α_t	h_{dev}	h_{vol}	h_{chem}
(-)	(MPa)	(MPa)	(-)	(-)	(-)	(-)	(-)	(-)	(MPa)	(-)	(-)	(-)	(-)	(-)	(-)
0.003	3500	1	1.4	1	0.05	0.9	0.55	1	40	6.2	0	0.1	55	55	5695

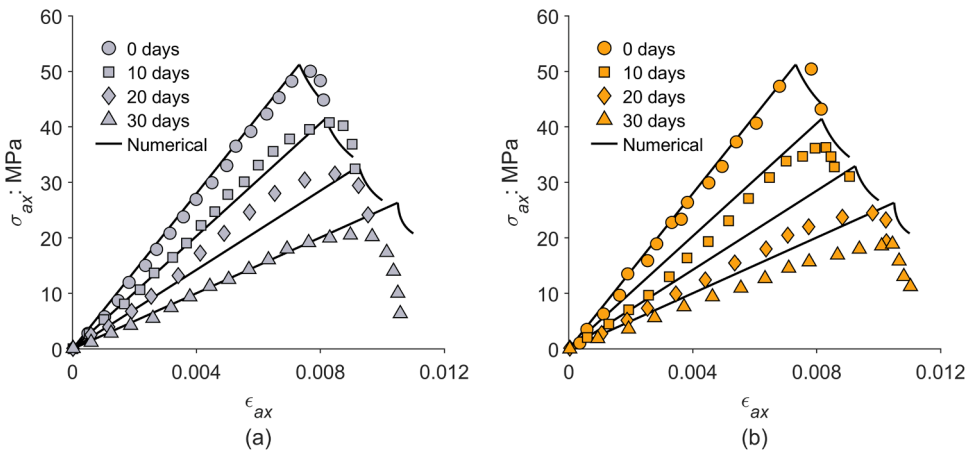

Fig. 10. Comparison between model predictions and experimental data for intact Longmaxi Shale in uniaxial compression tests after exposure to dissolved (a) liquid and (b) supercritical CO_2-saturated NaCl solution.

relevant than observed in the experimental tests. Experimental tests are necessarily performed at small loading periods; however, the results shall be interpreted using constitutive models capable of capturing strain-rate effects to scale them to the larger periods expected in the field. The model appears to be effective in capturing the experimental results of tests performed at different strain rates, although further validation is required at seasonal frequencies.

Effective use of the elasto-plastic framework in the context of CO_2 storage requires its coupling with geochemical processes. Strength and stiffness progressively decrease as dissolved CO_2 diffuses into the caprock formation and dissolution takes place. In the timescale of laboratory experiments, the dominant geochemical process has been shown to be the dissolution of carbonatic minerals. The reproduction of the impact of chemical changes on the mechanical behaviour was achieved by extending the model to include a chemical degradation mechanism that adopts the calcite mass fraction as an internal variable controlling the degree of damage. This leads to the definition of a flexible chemo-mechanical model that is not based on hidden chemical assumptions (i.e. open system, where the dissolved mass is completely removed), but capable of dealing with the input directly provided by geochemical interactions. The calcite mass fraction was obtained through a reactive transport model capable of reproducing a consistent chemical scenario which tracks the transport of dissolved CO_2, water acidification, and mineral dissolution. The enhanced model was shown to be effective in reproducing the impact of CO_2 exposure on the strength and stiffness of a Chinese Shale for different time intervals.

While the framework is kept simple to limit the number of parameters and to make it accessible for industrial applications for large-scale reservoir studies, it proved to be accurate and versatile enough for the new challenges of energy geomechanics presented in the paper.

Notation

A	amplitude of the cyclic triaxial loading
a_b	ratio between current and initial value of b
b	material structure internal variable
b_o	initial value of b
$\boldsymbol{D^e}$	fourth-order elasticity tensor
E_b	Young's modulus of structured material
E_g	Young's modulus of remoulded material
E_h	Young's modulus for loading in the horizontal direction in cross anisotropy
E_v	Young's modulus for loading in the vertical direction in cross anisotropy
e	void ratio
e_o	initial void ratio
f	yield function in elasto-plasticity
f_d	dynamic surface in elasto-viscoplasticity
f_r	reference surface in elasto-viscoplasticity
G	shear modulus
G^*	shear modulus for loading in the vertical direction in cross anisotropy
G_b	shear modulus of structured material
G_g	shear modulus of remoulded material
g	plastic potential function
H	hardening modulus
H_d	component of the hardening modulus related to the plastic strain
h	damage internal variable
h_{chem}	parameter for the destructuration induced by chemical reactions
h_{dev}	parameter for the destructuration induced by deviatoric plastic strain
h_o	initial value of the damage variable
h_{vol}	parameter for the destructuration induced by volumetric plastic strain
J	cross anisotropic elastic parameter
K	bulk modulus
K^*	bulk modulus for loading in the vertical direction in cross anisotropy
K_b	bulk modulus of the structured material
$K_{eq,calc}$	equilibrium constant of calcite dissolution
K_g	bulk modulus of remoulded material
k^{acid}	empirical specific dissolution rate for acid reaction
k^{carb}	empirical specific dissolution rate for base reaction
$k^{neutral}$	empirical specific dissolution rate for neutral reaction
M	critical state stress ratio in $p' - q$ space
m_b	specific dissolved mass
m_{b0}	initial value of m_b
N_f	number of cycles to failure
PI	plasticity index
p'	mean effective stress
p_c	preconsolidation pressure
p_{cb}	preconsolidation pressure with material structure
$p_{cb,0}$	initial value of p_{cb}
p^d_{cb}	preconsolidation pressure with material structure for dynamic yield surface
p^r_{cb}	preconsolidation pressure with material structure for reference yield surface
$p^r_{cb,0}$	initial value of p^r_{cb}
p'_o	initial mean consolidation pressure

p_t	tensile strength of the structured material
p_t^d	tensile strength of the structured material for dynamic yield surface
p_t^r	tensile strength of the structured material for reference yield surface
q	deviatoric stress
$q_{\max}$	maximum deviatoric stress in cyclic triaxial loading
q_{mean}	mean deviatoric stress in cyclic triaxial loading
q_{peak}	peak shear strength
r_{CaCO_3}	total rate of reacting calcite dissolution
$r_{CaCO_3}^{diss}$	dissolving component of r_{CaCO_3}
$r_{CaCO_3}^{prec}$	reprecipitating component of r_{CaCO_3}
S_{CaCO_3}	specific surface of calcite
T	period of the sinusoidal cyclic triaxial loading
t	time
$V_{m,CaCO_3}$	molar volume of calcite
w_L	liquid limit
w_P	plastic limit
α	cross anisotropy parameter
α_d	material parameter in distribution of E_b and E_g
α_y	parameter influencing shape of yield surface
α_{VN}	normalization factor of the viscoplastic flow rule as in Vermeer and Neher[93]
α_t	parameter relating tensile strength and pre consolidation pressure
β_y	parameter influencing shape of plastic potential surface
$\boldsymbol{\varepsilon}$	strain tensor
$\boldsymbol{\varepsilon}^e$	elastic strain tensor
$\boldsymbol{\varepsilon}^p$	plastic strain tensor
ε_{dev}^e	deviatoric component of $\boldsymbol{\varepsilon}^e$
ε_{vol}^e	volumetric component of $\boldsymbol{\varepsilon}^e$
ε_{dev}^p	deviatoric component of $\boldsymbol{\varepsilon}^p$
ε_{vol}^p	volumetric component of $\boldsymbol{\varepsilon}^p$
ε_{ax}	axial strain
$\bar{\varepsilon}_{ax,c}$	average axial strain applied during a quarter of the cyclic loading
$\boldsymbol{\varepsilon}^{vp}$	viscoplastic strain tensor
ε_{vol}^{vp}	volumetric component of $\boldsymbol{\varepsilon}^{vp}$
$\bar{\varepsilon}_{vol}^{vp}$	volumetric component of viscoplastic strain tensor at reference time τ
$\varepsilon_{vol}^{e,mec}$	volumetric contribution of mechanical loading in ε_{vol}^e
$\varepsilon_{vol}^{e,chem}$	volumetric contribution of bonding material mass in ε_{vol}^e
$\varepsilon_{dev}^{e,chem}$	deviatoric contribution of bonding material mass in ε_{vol}^e
κ	slope of unloading-reloading line in e -lnp' plane
κ^*	modified swelling index
κ_{chem}	parameter relating $d\varepsilon_{vol}^{e,chem}$ and $\dot{m}_b$
λ	slope of compression line in e -lnp' plane
λ^*	modified compression index
Λ	plastic multiplier
μ^*	creep index
ν_{vh}	Poisson's ratio for loading in the vertical direction in cross anisotropy
ξ	deviatoric hardening variable
$\rho_{s,calc}$	solid density of calcite
$\boldsymbol{\sigma}'$	effective stress tensor
σ_v'	effective vertical stress
τ	reference time in the viscoplastic constitutive model
ϕ	porosity
ϕ_{CaCO_3}	calcite volumetric fraction
$\phi_{non-reac}$	volume fraction of the non-reactive grains
$\phi_{CaCO_3,b}$	dissolved calcite mass
ψ_k	set of k internal variables

CRediT authorship contribution statement

Andrea Ciancimino: Writing – original draft, Visualization, Methodology, Investigation, Data curation, Conceptualization. **Gabriele Della Vecchia:** Writing – original draft, Supervision, Methodology, Funding acquisition, Conceptualization. **Giorgio Volonté:** Writing – review & editing, Project administration. **Liliana Gramegna:** Writing – original draft, Visualization, Software, Methodology, Data curation. **Trishala Daka:** Writing – original draft, Visualization, Software, Methodology, Data curation. **Guido Musso:** Writing – original draft, Supervision, Methodology, Funding acquisition, Conceptualization.

Declaration of Competing Interest

The authors declare that they have no known competing financial interests or personal relationships that could have appeared to influence the work reported in this paper.

Acknowledgments

Funding for the numerical study was provided by ENI SpA within the projects "Ecophysics" and "Hynergy". The authors gratefully thank Eni SpA for the authorization to publish this work. The activity of T. Daka was partially financed by the Italian Ministry for Education, University and Research (MIUR) through the DM1061.

Data availability

Data will be made available on request.

References

1. Teatini P, Castelletto N, Ferronato M, et al. Geomechanical response to seasonal gas storage in depleted reservoirs: A case study in the Po River basin, Italy. *J Geophys Res: Earth Surf*. 2011;116(2). https://doi.org/10.1029/2010JF001793.
2. Bruant RG, Guswa Jr AJ, Celia MA, Peters CA. Safe storage of CO2 in deep saline aquifers. *Environ Sci Technol*. 2002;36(11), 240A-245A.
3. Heinemann N, Alcalde J, Miocic JM, et al. Enabling large-scale hydrogen storage in porous media-the scientific challenges. *Energy Environ Sci*. 2021;14(2):853–864. https://doi.org/10.1039/d0ee03536j.
4. Okoroafor ER, Saltzer SD, Kovscek AR. Toward underground hydrogen storage in porous media: Reservoir engineering insights. *Int J Hydrog Energy*. 2022;47(79): 33781–33802. https://doi.org/10.1016/j.ijhydene.2022.07.239.
5. Miocic J, Heinemann N, Edlmann K, Scafidi J, Molaei F, Alcalde J. Underground hydrogen storage: a review. *Geol Soc Spec Publ*. 2023;528:73–86. https://doi.org/10.1144/SP528-2022-88.
6. Rutqvist J. The geomechanics of CO 2 storage in deep sedimentary formations. *Geotech Geol Eng*. 2012;30(3):525–551. https://doi.org/10.1007/s10706-011-9491-0.
7. Vilarrasa V, Bolster D, Olivella S, Carrera J. Coupled hydromechanical modeling of CO2 sequestration in deep saline aquifers. *Int J Greenh Gas Control*. 2010;4(6): 910–919. https://doi.org/10.1016/j.ijggc.2010.06.006.
8. Lavrov, A. (2016). Dynamics of stresses and fractures in reservoir and cap rock under production and injection. Paper presented at the Energy Procedia.
9. Musso G, Volonté G, Gemelli F, et al. Evaluating the subsidence above gas reservoirs with an elasto-viscoplastic constitutive law. Laboratory evidences and case histories. *Geomech Energy Environ*. 2021;28. https://doi.org/10.1016/j.gete.2021.100246.
10. Nagel NB. Compaction and subsidence issues within the petroleum industry: From Wilmington to Ekofisk and beyond. *Phys Chem Earth, Part A: Solid Earth Geod*. 2001;26(1-2):3–14. https://doi.org/10.1016/S1464-1895(01)00015-1.
11. Settari A, Walters DA. Advances in coupled geomechanical and reservoir modeling with applications to reservoir compaction. *SPE J*. 2001;6(3):334–342. https://doi.org/10.2118/74142-PA.
12. Hettema MHH, Schutjens PMTM, Verboom BJM, Gussinklo HJ. Production-induced compaction of a sandstone reservoir: The strong influence of stress path. *SPE Reserv Eval Eng*. 2000;3(4):342–347. https://doi.org/10.2118/65410-PA.
13. Liu Q, Maroto-Valer MM. Investigation of the pH effect of a typical host rock and buffer solution on CO2 sequestration in synthetic brines. *Fuel Process Technol*. 2010;91(10):1321–1329. https://doi.org/10.1016/j.fuproc.2010.05.002.
14. Gunter WD, Perkins EH, Hutcheon I. Aquifer disposal of acid gases: Modelling of water-rock reactions for trapping of acid wastes. *Appl Geochem*. 2000;15(8): 1085–1095. https://doi.org/10.1016/S0883-2927(99)00111-0.
15. Gherardi F, Xu T, Pruess K. Numerical modeling of self-limiting and self-enhancing caprock alteration induced by CO2 storage in a depleted gas reservoir. *Chem Geol*. 2007;244(1-2):103–129. https://doi.org/10.1016/j.chemgeo.2007.06.009.

16. Armitage PJ, Faulkner DR, Worden RH. Caprock corrosion. *Nat Geosci*. 2013;6(2):79–80. https://doi.org/10.1038/ngeo1716.
17. Kharaka YK, Cole DR, Hovorka SD, Gunter WD, Knauss KG, Freifeld BM. Gas-water-rock interactions in Frio Formation following CO2 injection: Implications for the storage of greenhouse gases in sedimentary basins. *Geology*. 2006;34(7):577–580. https://doi.org/10.1130/G22357.1.
18. Wigley M, Kampman N, Dubacq B, Bickle M. Fluid-mineral reactions and trace metal mobilization in an exhumed natural CO2 reservoir, Green River, Utah. *Geology*. 2012;40(6):555–558. https://doi.org/10.1130/G32946.1.
19. Vafaie A, Cama J, Soler JM, Kivi IR, Vilarrasa V. Chemo-hydro-mechanical effects of CO2 injection on reservoir and seal rocks: A review on laboratory experiments. *Renew Sustain Energy Rev*. 2023;178, 113270. https://doi.org/10.1016/j.rser.2023.113270.
20. Berrezueta E, Kovacs T, Herrera-Franco G, et al. Laboratory studies on CO2-brine-rock interaction: an analysis of research trends and current knowledge. *Int J Greenh Gas Control*. 2023;123, 103842. https://doi.org/10.1016/j.ijggc.2023.103842.
21. Vilarrasa, V., Olivella, S., & Carrera, J. (2011). Geomechanical stability of the caprock during CO2 sequestration in deep saline aquifers. Paper presented at the Energy Procedia.
22. Boulin PF, Bretonnier P, Vassil V, Samouillet A, Fleury M, Lombard JM. Sealing efficiency of caprocks: Experimental investigation of entry pressure measurement methods. *Mar Pet Geol*. 2013;48:20–30. https://doi.org/10.1016/j.marpetgeo.2013.07.010.
23. Vespo, V.S., Messori, A., & Musso, G. (2024). Threshold capillary pressure of caprocks for CO2 storage: numerical insight on the dynamic and residual method. International Journal of Greenhouse Gas Control(accepted).
24. Minardi A, Stavropoulou E, Kim T, Ferrari A, Laloui L. Experimental assessment of the hydro-mechanical behaviour of a shale caprock during CO2 injection. *Int J Greenh Gas Control*. 2021;106. https://doi.org/10.1016/j.ijggc.2020.103225.
25. Parisio F, Samat S, Laloui L. Constitutive analysis of shale: a coupled damage plasticity approach. *Int J Solids Struct*. 2015;75-76:88–98. https://doi.org/10.1016/j.ijsolstr.2015.08.003.
26. De Bellis ML, Della Vecchia G, Ortiz M, Pandolfi A. A linearized porous brittle damage material model with distributed frictional-cohesive faults. *Eng Geol*. 2016;215:10–24. https://doi.org/10.1016/j.enggeo.2016.10.010.
27. Parisio F, Laloui L. Plastic-damage modeling of saturated quasi-brittle shales. *Int J Rock Mech Min Sci*. 2017;93:295–306. https://doi.org/10.1016/j.ijrmms.2017.01.016.
28. De Bellis ML, Della Vecchia G, Ortiz M, Pandolfi A. A multiscale model of distributed fracture and permeability in solids in all-round compression. *J Mech Phys Solids*. 2017;104:12–31. https://doi.org/10.1016/j.jmps.2017.03.017.
29. Gens, A., & Nova, R. (1993). Conceptual bases for a constitutive model for bonded soils and weak rocks. Paper presented at the Int. Symp. On Geomechanical Engineering of Hard Soils and Soft Rocks, Athens.
30. Nova R, Castellanza R, Tamagnini C. A constitutive model for bonded geomaterials subject to mechanical and/or chemical degradation. *Int J Numer Anal Methods Geomech*. 2003;27(9):705–732. https://doi.org/10.1002/nag.294.
31. Baudet B, Stallebrass S. A constitutive model for structured clays. *Geotechnique*. 2004;54(4):269–278. https://doi.org/10.1680/geot.2004.54.4.269.
32. Uchida S, Soga K, Yamamoto K. Critical state soil constitutive model for methane hydrate soil. *J Geophys Res: Solid Earth*. 2012;117(3). https://doi.org/10.1029/2011JB008661.
33. Taiebat M, Dafalias YF, Peek R. A destructuration theory and its application to SANICLAY model. *Int J Numer Anal Methods Geomech*. 2010;34(10):1009–1040. https://doi.org/10.1002/nag.841.
34. Gajo A, Cecinato F, Hueckel T. Chemo-mechanical modeling of artificially and naturally bonded soils. *Geomech Energy Environ*. 2019;18:13–29. https://doi.org/10.1016/j.gete.2018.11.005.
35. Gajo A, Cecinato F, Hueckel T. A micro-scale inspired chemo-mechanical model of bonded geomaterials. *Int J Rock Mech Min Sci*. 2015;80:425–438. https://doi.org/10.1016/j.ijrmms.2015.10.001.
36. Sivasithamparam N, Castro J. Undrained cylindrical cavity expansion in clays with fabric anisotropy and structure: Theoretical solution. *Comput Geotech*. 2020;120. https://doi.org/10.1016/j.compgeo.2019.103386.
37. di Prisco C, Flessati L. Progressive failure in elastic-viscoplastic media: From theory to practice. *Geotechnique*. 2021;71(2):153–169. https://doi.org/10.1680/jgeot.19.P.045.
38. Ghosh Dastider A, Basu P, Chatterjee S. Numerical Implementation of a Stress-Anisotropy Model for Bearing Capacity Analysis of Circular Footings in Clays Prone to Destructuration. *J Geotech Geoenviron Eng*. 2021;147(5). https://doi.org/10.1061/(ASCE)GT.1943-5606.0002482.
39. Zeng B, Zhang D, Xu J, Xu T, Wang A, Yang S. Numerical simulation of horizontal bearing characteristics of cement-soil reinforced rock-socketed steel pipe monopile considering cementation damage. *Comput Geotech*. 2023;162. https://doi.org/10.1016/j.compgeo.2023.105626.
40. Seidalinov G, Taiebat M. Bounding surface SANICLAY plasticity model for cyclic clay behavior. *Int J Numer Anal Methods Geomech*. 2014;38(7):702–724. https://doi.org/10.1002/nag.2229.
41. Palmieri F, Taiebat M. An activation mechanism for cyclic degradation of clays in bounding surface plasticity. *Int J Numer Anal Methods Geomech*. 2024. https://doi.org/10.1002/nag.3728.
42. Shi Z, Buscarnera G, Finno RJ. Simulation of cyclic strength degradation of natural clays via bounding surface model with hybrid flow rule. *Int J Numer Anal Methods Geomech*. 2018;42(14):1719–1740. https://doi.org/10.1002/nag.2813.
43. Tafili M, Triantafyllidis T. AVISA: anisotropic visco-ISA model and its performance at cyclic loading. *Acta Geotech*. 2020;15(9):2395–2413. https://doi.org/10.1007/s11440-020-00925-9.
44. Anandarajah A, Dafalias YF. Bounding surface plasticity. III: Application to anisotropic cohesive soils. *J Eng Mech*. 1986;112(12):1292–1318. https://doi.org/10.1061/(ASCE)0733-9399(1986)112:12(1292).
45. Dafalias YF. Bounding surface plasticity. I: Mathematical foundation and hypoplasticity. *J Eng Mech*. 1986;112(9):966–987. https://doi.org/10.1061/(ASCE)0733-9399(1986)112:9(966).
46. Dafalias YF, Herrmann LR. Bounding surface plasticity. II: Application to isotropic cohesive soils. *J Eng Mech*. 1986;112(12):1263–1291. https://doi.org/10.1061/(ASCE)0733-9399(1986)112:12(1263).
47. Kaliakin VN, Dafalias YF. Simplifications to the bounding surface model for cohesive soils. *Int J Numer Anal Methods Geomech*. 1989;13(1):91–100. https://doi.org/10.1002/nag.1610130108.
48. Gajo A, Colleselli F. Calculated and observed behaviour of clayey soil under cyclic loading beneath preloading embankments for oil tanks. *Can Geotech J*. 2009;46(5):494–512. https://doi.org/10.1139/T09-001.
49. Seidalinov, G., & Taiebat, M. (2019). Nonlinear seismic site response analysis of soft clay deposits using saniclay-b constitutive model. Paper presented at the Earthquake Geotechnical Engineering for Protection and Development of Environment and Constructions- Proceedings of the 7th International Conference on Earthquake Geotechnical Engineering, 2019.
50. Antoniou M, Gelagoti F, Herzog R, Kourkoulis R, Anastasopoulos I. Offshore foundations in low-plasticity cohesive soils: Cyclic degradation experimental evidence and simplified numerical analysis. *Ocean Eng*. 2024;292, 116495. https://doi.org/10.1016/j.oceaneng.2023.116495.
51. Heide D, von Bremen L, Greiner M, Hoffmann C, Speckmann M, Bofinger S. Seasonal optimal mix of wind and solar power in a future, highly renewable Europe. *Renew Energy*. 2010;35(11):2483–2489. https://doi.org/10.1016/j.renene.2010.03.012.
52. Lefebvre G, LeBoeuf D. Rate effects and cyclic loading of sensitive clays. *J Geotech Eng*. 1987;113(5):476–489. https://doi.org/10.1061/(ASCE)0733-9410(1987)113:5(476).
53. Ciancimino, A., Cosentini, R.M., Foti, S., Messori, A., Ullah, H., Volonté, G., & Musso, G. (accepted). A preliminary investigation on the mechanical behaviour of a stiff Italian clay in the context of hydrogen storage. Geomechanics for Energy and the Environment.
54. Al-Bazali T, Zhang J, Chenevert ME, Sharma MM. Experimental and numerical study on the impact of strain rate on failure characteristics of shales. *J Pet Sci Eng*. 2008;60(3-4):194–204. https://doi.org/10.1016/j.petrol.2007.09.001.
55. Hou Z, Gutierrez M, Ma S, Almrabat A, Yang C. Mechanical Behavior of Shale at Different Strain Rates. *Rock Mech Rock Eng*. 2019;52(10):3531–3544. https://doi.org/10.1007/s00603-019-01807-7.
56. Lagioia R, Nova R. An experimental and theoretical study of the behaviour of a calcarenite in triaxial compression. *Geotechnique*. 1995;45(4):633–648. https://doi.org/10.1680/geot.1995.45.4.633.
57. Fernandez-Merodo JA, Castellanza R, Mabssout M, Pastor M, Nova R, Parma M. Coupling transport of chemical species and damage of bonded geomaterials. *Comput Geotech*. 2007;34(4):200–215. https://doi.org/10.1016/j.compgeo.2007.02.008.
58. Ciantia MO, di Prisco C. Extension of plasticity theory to debonding, grain dissolution, and chemical damage of calcarenites. *Int J Numer Anal Methods Geomech*. 2016;40(3):315–343. https://doi.org/10.1002/nag.2397.
59. Zou Y, Li S, Ma X, Zhang S, Li N, Chen M. Effects of CO2–brine–rock interaction on porosity/permeability and mechanical properties during supercritical-CO2 fracturing in shale reservoirs. *J Nat Gas Sci Eng*. 2018;49:157–168. https://doi.org/10.1016/j.jngse.2017.11.004.
60. Borja RI, Yin Q, Zhao Y. Cam-Clay plasticity. Part IX: On the anisotropy, heterogeneity, and viscoplasticity of shale. *Comput Methods Appl Mech Eng*. 2020;360. https://doi.org/10.1016/j.cma.2019.112695.
61. Farhat F, Shen WQ, Shao JF. A micro-mechanics based viscoplastic model for clayey rocks. *Comput Geotech*. 2017;89:92–102. https://doi.org/10.1016/j.compgeo.2017.04.014.
62. Sari M, Alevizos S, Poulet T, Lin J, Veveakis M. A visco-plastic framework for interface processes in sedimentary reservoir rocks at HPHT conditions. *Geomech Energy Environ*. 2020;22. https://doi.org/10.1016/j.gete.2019.100165.
63. Perzyna P. The constitutive equations for rate sensitive plastic materials. *Q Appl Math*. 1963;20(4):321–332.
64. Perzyna P. Fundamental Problems in Viscoplasticity. *Adv Appl Mech*. 1966;9(C):243–377. https://doi.org/10.1016/S0065-2156(08)70009-7.
65. Rassouli FS, Zoback MD. Comparison of Short-Term and Long-Term Creep Experiments in Shales and Carbonates from Unconventional Gas Reservoirs. *Rock Mech Rock Eng*. 2018;51(7):1995–2014. https://doi.org/10.1007/s00603-018-1444-y.
66. Sone H, Zoback MD. Time-dependent deformation of shale gas reservoir rocks and its long-term effect on the in situ state of stress. *Int J Rock Mech Min Sci*. 2014;69:120–132. https://doi.org/10.1016/j.ijrmms.2014.04.002.
67. Mighani S, Bernabé Y, Boulenouar A, Mok U, Evans B. Creep Deformation in Vaca Muerta Shale From Nanoindentation to Triaxial Experiments. *J Geophys Res: Solid Earth*. 2019;124(8):7842–7868. https://doi.org/10.1029/2019JB017524.
68. Yin ZY, Chang CS, Karstunen M, Hicher PY. An anisotropic elastic-viscoplastic model for soft clays. *Int J Solids Struct*. 2010;47(5):665–677. https://doi.org/10.1016/j.ijsolstr.2009.11.004.

69. Kutter BL, Sathialingam N. Elastic-viscoplastic modelling of the rate-dependent behaviour of clays. *Geotechnique*. 1992;42(3):427–441. https://doi.org/10.1680/geot.1992.42.3.427.
70. Leoni M, Karstunen M, Vermeer PA. Anisotropic creep model for soft soils. *Geotechnique*. 2008;58(3):215–226. https://doi.org/10.1680/geot.2008.58.3.215.
71. Mánica MA, Gens A, Ovando-Shelley E, Botero E, Vaunat J. An effective combined framework for modelling the time-dependent behaviour of soft structured clays. *Acta Geotech*. 2021;16(2):535–550. https://doi.org/10.1007/s11440-020-01025-4.
72. Wood, D.M. (2004). Geotechnical modelling (C. Press Ed.): CRC press.
73. Panteghini A, Lagioia R. An extended modified Cam-Clay yield surface for arbitrary meridional and deviatoric shapes retaining full convexity and double homothety. *Geotechnique*. 2018;68(7):590–601. https://doi.org/10.1680/jgeot.17.P.016.
74. Cattaneo F, Della Vecchia G, Jommi C. Evaluation of numerical stress-point algorithms on elastic–plastic models for unsaturated soils with hardening dependent on the degree of saturation. *Comput Geotech*. 2014;55:404–415. https://doi.org/10.1016/j.compgeo.2013.09.018.
75. Adachi T, Oka F, Hirata T, et al. Stress-strain behavior and yielding characteristics of eastern Osaka clay. *Soils Found*. 1995;35(3):1–13. https://doi.org/10.3208/sandf.35.1.
76. Graham J, Houlsby GT. Anisotropic elasticity of a natural clay. *Geotechnique*. 1983;33(2):165–180. https://doi.org/10.1680/geot.1983.33.2.165.
77. Giger SB, Ewy RT, Favero V, Stankovic R, Keller LM. Consolidated-undrained triaxial testing of Opalinus Clay: Results and method validation. *Geomech Energy Environ*. 2018;14:16–28. https://doi.org/10.1016/j.gete.2018.01.003.
78. Liu L, Martin D, Giger SB, Chalaturnyk R. Assessment of Anisotropic Elastic Parameters Using Laboratory Triaxial and In-Situ Pressuremeter Tests in Opalinus Clay. *Rock Mech Rock Eng*. 2024;57(11):10153–10165. https://doi.org/10.1007/s00603-024-04030-1.
79. Favero V, Ferrari A, Laloui L. Anisotropic Behaviour of Opalinus Clay Through Consolidated and Drained Triaxial Testing in Saturated Conditions. *Rock Mech Rock Eng*. 2018;51(5):1305–1319. https://doi.org/10.1007/s00603-017-1398-5.
80. Bertrand F, Collin F. Anisotropic modelling of Opalinus Clay behaviour: From triaxial tests to gallery excavation application. *J Rock Mech Geotech Eng*. 2017;9(3):435–448. https://doi.org/10.1016/j.jrmge.2016.12.005.
81. Ciancimino A, Cosentini RM, Foti S, et al. A preliminary investigation on the mechanical behaviour of a stiff Italian clay in the context of hydrogen storage. *Geomech Energy Environ*. 2024;38. https://doi.org/10.1016/j.gete.2024.100562.
82. Schmitt DR, Zoback MD. Diminished pore pressure in low-porosity crystalline rock under tensional failure: apparent strengthening by dilatancy. *J Geophys Res*. 1992;97(B1):273–288. https://doi.org/10.1029/91JB02256.
83. Brace WF, Paulding Jr BW, Scholz C. Dilatancy in the fracture of crystalline rocks. *J Geophys Res (1896-1977)*. 1966;71(16):3939–3953. https://doi.org/10.1029/JZ071i016p03939.
84. Hu DW, Zhang F, Shao JF. Experimental study of poromechanical behavior of saturated claystone under triaxial compression. *Acta Geotech*. 2014;9(2):207–214. https://doi.org/10.1007/s11440-013-0259-y.
85. Jeanne P, Zhang Y, Rutqvist J. Influence of hysteretic stress path behavior on seal integrity during gas storage operation in a depleted reservoir. *J Rock Mech Geotech Eng*. 2020;12(4):886–899. https://doi.org/10.1016/j.jrmge.2020.06.002.
86. Ahmadi-Naghadeh R, Liu T, Vinck K, et al. A laboratory characterisation of the response of intact chalk to cyclic loading. *Geotechnique*. 2022. https://doi.org/10.1680/jgeot.21.00198.
87. Sharma SS, Fahey M. Evaluation of cyclic shear strength of two cemented calcareous soils. *J Geotech Geoenviron Eng*. 2003;129(7):608–618. https://doi.org/10.1061/(ASCE)1090-0241(2003)129:7(608).
88. Ushev E, Jardine R. The behaviour of Bolders Bank glacial till under undrained cyclic loading. *Geotechnique*. 2022;72(1):1–19. https://doi.org/10.1680/jgeot.18.P.236.
89. Ciancimino A., Cosentini R.M., Foti S., Volontè G., Musso G. Experimental investigation on the monotonic and cyclic behaviour of a structured clay at high confinement. Geotechnique. Submitted.
90. Dafalias YF, Manzari MT, Papadimitriou AG. SANICLAY: Simple anisotropic clay plasticity model. *Int J Numer Anal Methods Geomech*. 2006;30(12):1231–1257. https://doi.org/10.1002/nag.524.
91. Lefebvre G, Pfendler P. Strain rate and preshear effects in cyclic resistance of soft clay. *J Geotech Eng*. 1996;122(1):21–26. https://doi.org/10.1061/(asce)0733-9410(1996)122:1(21).
92. Adachi T, Oka F. Constitutive equations for normally consolidated clay based on elasto-viscoplast. *icity Soils Found*. 1982;22(4):57–70. https://doi.org/10.3208/sandf1972.22.4_57.
93. Vermeer, P.A., & Neher, H.P. (1999). A soft soil model that accounts for creep. Paper presented at the Beyond 2000 in computational geotechnics. Ten Years of PLAXIS International. Proceedings of the international symposium, Amsterdam, March 1999.
94. Ghoussoub J, Leroy YM. Solid-fluid phase transformation within grain boundaries during compaction by pressure solution. *J Mech Phys Solids*. 2001;49(10):2385–2430. https://doi.org/10.1016/S0022-5096(01)00012-6.
95. Hu LB, Hueckel T. Creep of saturated materials as a chemically enhanced rate-dependent damage process. *Int J Numer Anal Methods Geomech*. 2007;31(14):1537–1565. https://doi.org/10.1002/nag.600.
96. Terzaghi, K. (1943). Theoretical soil mechanics. New York: John Wiley & Sons, Inc,.
97. Dadras-Ajirlou D, Grimstad G, Amiri SAG, Degago SA, Houlsby GT. Modified cam clay bounding surface hyper-viscoplastic model. *Geotech, Print*. 2024;0:1–41. https://doi.org/10.1680/jgeot.23.00308.
98. Fuentes W, Tafili M, Triantafyllidis T. An ISA-plasticity-based model for viscous and non-viscous clays. *Acta Geotech*. 2018;13(2):367–386. https://doi.org/10.1007/s11440-017-0548-y.
99. Berrezueta E, Moita P, Pedro J, et al. Laboratory experiments and modelling of the geochemical interaction of a gabbro-anorthosite with seawater and supercritical CO2: A mineral carbonation study. *Geoenergy Sci Eng*. 2023;228. https://doi.org/10.1016/j.geoen.2023.212010.
100. Liu F, Lu P, Griffith C, et al. CO2-brine-caprock interaction: Reactivity experiments on Eau Claire shale and a review of relevant literature. *Int J Greenh Gas Control*. 2012;7:153–167. https://doi.org/10.1016/j.ijggc.2012.01.012.
101. Gaus I, Azaroual M, Czernichowski-Lauriol I. Reactive transport modelling of the impact of CO2 injection on the clayey cap rock at Sleipner (North Sea). *Chem Geol*. 2005;217(3-4 SPEC. ISS.):319–337. https://doi.org/10.1016/j.chemgeo.2004.12.016.
102. Steefel CI, Lasaga AC. A coupled model for transport of multiple chemical species and kinetic precipitation/dissolution reactions with application to reactive flow in single phase hydrothermal systems. *Am J Sci*. 1994;294(5):529–592. https://doi.org/10.2475/ajs.294.5.529.
103. López-Vizcaíno R, Yustres Á, Cabrera V, Navarro V. A worksheet-based tool to implement reactive transport models in COMSOL Multiphysics. *Chemosphere*. 2021;266. https://doi.org/10.1016/j.chemosphere.2020.129176.
104. Plummer LN, Wigley TML, Parkhurst DL. Kinetics of calcite dissolution in CO2-water systems at 5 degree TO 60 degree C AND 0.0 TO 1.0 ATM CO2. *Am J Sci*. 1978;278(2):179–216.
105. Palandri, J.L., & Kharaka, Y.K. (2004). A Compilation of Rate Parameters of Water-Mineral Interaction Kinetics for Application to Geochemical Modeling. Menlo Park CA.
106. Molins S, Trebotich D, Miller GH, Steefel CI. Mineralogical and transport controls on the evolution of porous media texture using direct numerical simulation. *Water Resour Res*. 2017;53(5):3645–3661. https://doi.org/10.1002/2016WR020323.
107. Lyu Q, Long X, Ranjith PG, Tan J, Kang Y, Luo W. A damage constitutive model for the effects of CO2-brine-rock interactions on the brittleness of a low-clay shale. *Geofluids*. 2018;2018. https://doi.org/10.1155/2018/7321961.
108. Lyu Q, Ranjith PG, Long X, Ji B. Experimental investigation of mechanical properties of black shales after CO2-water-rock interaction. *Materials*. 2016;9(8). https://doi.org/10.3390/ma9080663.
109. Espinoza DN, Kim SH, Santamarina JC. CO2 geological storage - Geotechnical implications. *KSCE J Civ Eng*. 2011;15(4):707–719. https://doi.org/10.1007/s12205-011-0011-9.
110. Lu R, Nagel T, Poonoosamy J, et al. A new operator-splitting finite element scheme for reactive transport modeling in saturated porous media. *Comput Geosci*. 2022;163. https://doi.org/10.1016/j.cageo.2022.105106.
111. Gramegna L, Musso G, Messori A, Della Vecchia G. A reactive transport model for calcite-rich caprocks in the context of geological carbon storage. *Pap Presente Symp Energy Geotech*. 2023.
112. Cabrera V, López-Vizcaíno R, Yustres Á, Navarro V. Reactive transport model for bentonites in COMSOL multiphysics: Benchmark and validation exercise. *Chemosphere*. 2024;350. https://doi.org/10.1016/j.chemosphere.2023.141050.
113. Chen S, Chen S, Clementine U, Liu Y, Zhang C. Reservoir diffusion properties of the Longmaxi shale in Shizhu area, Southern Sichuan basin, China. *Energy Explor Exploit*. 2018;36(5):1086–1102. https://doi.org/10.1177/0144598717751182.